IIB Project Final Report:

Molecular Electronic Devices

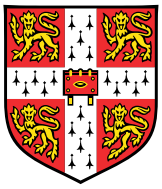

Jonathan Shaw

Magdalene College

2023

supervised by Colm Durkan

Abstract

Current silicon-based devices are experiencing limitations in downsizing. There is therefore a need for new design methods. Molecular devices show potential through their nanoscale dimensions, low power dissipation and desirable properties that are achievable through elaborate synthetic methods. The primary challenges lie within fabricating the nanogaps to insert the organic molecules into and controlling the metal-molecule interface, necessitating improved fabrication strategies.

This project addresses the fabrication of organic molecular devices in three stages: first focused ion beam (FIB) technology is utilized for nanowire deposition; second, electromigration and Joule heating, induced through voltage ramps in the nanowires, for nanogap formation; and finally the addition of Organic molecules to the system under an electric field to fabricate molecules molecular devices. Thus addressing the challenges associated with downsizing silicon-based electronic devices by exploring bottom-up approaches, in the form of molecular devices, holds promise to achieve higher density and cost-effective circuitry.

The utilisation of FIB technology overcomes the primary challenges of nanogap formation, with current capabilities of Helium ion beam microscopy enabling the fabrication of sub-50 nm structures without a photoresist. Thin wires are desirable for more reliable and consistent failure characteristics. By using a gas injection system to distribute a flux of precursor gas an ion beam can break down the gas molecules adsorbed to the surface. This process is commonly referred to as Focused-Ion-Beam-Induced-Deposition (FIBID).

Sets of platinum electrodes on a SiO_2 substrate were used for testing with gaps varying from $2 - 10\mu m$ in length. The precursor gas trimethyl (methylcyclopentadienyl) platinum was used to form the nanowires, broken down by ion beams. Gallium, neon and helium ion beams were tested, with further imaging done using a scanning electron microscope. The nanowires were patterned to bridge the gap between the two electrodes. The resulting structure is broadly comprised of interstitial platinum clusters in an amorphous carbon matrix. Nanogap failure was induced through voltage ramps ranging from 0-20V. After formation, the organic molecule 1,5 diamino 2 methyl pentane was added to the system whilst a voltage was applied to the electrodes via a set of probes connected up to a source measurement unit.

Successful imaging of various samples demonstrated the helium FIB system's high-resolution visualization capabilities. As expected, neon and gallium FIB imaging provided lower-resolution images typically forming wider nanowire structures. Nanowire deposition using FIB yielded well-defined nanowires, of varying dimensions. Variability in topology and deposition characteristics. however, poses challenges for large-scale yield. The nanowire structures exhibited promising electrical properties, as indicated by voltage plots obtained during testing. Non-linear characteristics were observed, reflecting the microstructure and underlying transport mechanisms. The fabrication of nanowires opened up avenues for further research and extension in various nanoscale applications.

The formation of nanogaps using voltage ramps was a variable process: electromigration contributed towards failure, yet there were key signs of the nanowire structure melting. This highlights the intricacies and technical challenges associated with the nanogap formation process, necessitating further investigation and optimization of this process. Additionally, the incorporation of organic molecules onto the fabricated nanowires using FIB yielded charging characteristics observed in hysteresis I(V) plots. The desired diode-like characteristics were insufficient for functionalization and potential applications in electronic devices. Alternative techniques or approaches are required to effectively incorporate organic molecules.

Directions for future research were identified based on the findings. Extended research into platinum FIBID nanowire failure mechanisms through in-situ observations of microstructure re-arrangement during failure was suggested. The use of transmission electron microscopy (TEM) imaging to analyze microstructures could provide further insights. Alternative test chips with thinner electrode contacts were proposed to overcome fabrication challenges. Electron beam lithography and helium ion microscopy were mentioned as potential alternatives for nanogap formation and wire failure promotion.

In conclusion, the successful fabrication of nanowires using FIB technology and their promising electrical properties offers valuable insights and possibilities for fu- ture research. However, challenges remain in nanogap formation (particularly for nanowires formed via FIBID due to the variable composition and microstructure) and the incorporation of organic molecules. Addressing these limitations and building upon the successes and failures of this project promises to advance the field of nanoscale device fabrication, leading to improved molecular devices and their potential integration into future electronic systems.

Keywords: *Focused ion beam, nanowire deposition, nanogap formation, molecular devices, nanoscale fabrication, organic molecules, molecular electronic device.*

Table of Contents

Glossary

dwell time the time an ion beam remains at discrete points in a pattern. 27
electromigration the transport of material resulting from momentum transfer between electrons and ions. 6, 11, 42
eucentric position the working distance that maintains focus when the sample is tilted. 16, 17
Joule heating known as resistive heating, whereby current flowing through a conductor generates heat. 6
nanofabrication the design process regarding materials on a nanometer scale. 3
probe size the diameter of the ion beam at the point of contact with a surface. 14
torr unit of pressure, defined as 1/760 of an atmosphere $\approx$ 133.32 Pa. 18
trimer three atom tip (of the tungsten gun tip on the Orion system). 38
working distance distance from lens 2 when focused. 16

Acronyms

BIV Best Imaging Voltage. 23
EBID Electron-Beam-Induced-Deposition. 6, 10, 12, 30
ETD Everhart-Thornley Detector. 14, 17, 27
FEBID Focused-Electron-Beam-Induced-Deposition, same as EBID. 10
FET Field Effect Transistor. 44
FIB Focused Ion Beam. 3, 8, 9, 11, 13, 16, 19, 26, 27, 43
FIBID Focused-Ion-Beam-Induced-Deposition, same as IBID. 10, 29–31, 33, 34, 36, 37, 39
GFIS Gas Field Ion Source. 11, 16, 39
GIS Gas Injection System. 13, 16, 17, 19, 23, 31, 34
HIM Helium-ion Microscopy. 14, 44
IBID Ion-Beam-Induced-Deposition. 1, 6, 9, 11, 12, 24, 29, 39, 42
MCBJ Mechanically Controlled Break Junction. 6, 7
MEMS-BJ Micro-Electromechanical-System Break-Junction. 6
MOSFET Metal-Oxide-Semiconductor Field-Effect Transistor. 4
SE Secondary Electrons. 10
SEM Scanning Electron Microscope. 12, 18, 19, 29, 32, 36, 38, 43
SMU Source Measurement Unit. 20, 22
STM-BJ Scanning Tunneling Microscope Break-Junction. 6, 7
TEM Tunnelling Electron Microscope. 40, 46

1 Introduction

1.1 Overview

Silicon-based devices have reached the molecular scale. The gate lengths of transistors found in common microprocessors typically range from 20 to 30 nm. State-of-the-art transistors have gate lengths of 3nm with recent research claiming gate lengths less than 1nm[1]. However, it is becoming increasingly difficult to down-scale the size of these electronic devices. This combined with low yield and exponentially increasing costs of new devices makes them unviable for large-scale manufacturing. It is apparent that new design methods are still required, with opportunity in bottom-up approaches [2]. Molecular devices are a particularly promising contender to continue the trend in minimization, with new fabrication methods being continually developed to show advantages over traditional silicon-based designs. The primary benefit of molecular devices comes with the ease of synthesis of identical molecules. These molecules lie on a scale of several nanometers across, giving potential for high-density circuitry. Desirable electrical, thermal, mechanical and optical properties can be achieved through elaborate synthetic methods making them ideal for integrated circuits. The cost of molecular devices can be substantially less than alternate methods as a result of new fabrication techniques and lower power dissipation from the molecules themselves[3]. These advantages make molecular devices a particularly exciting field however the primary challenges lie within fabricating the nanogaps in which the molecules are deposited and controlling the metal-molecule interface, for which improved fabrication strategies are required.

The report explores the utilization of nanofabrication, specifically Focused Ion Beam (FIB), capabilities to form repeatable nanowire structures and molecular electronic devices. Electromigration and Joule heating, induced by current flow are used to form nanogap junctions in the aforementioned nanowires. Inserting the asymmetric organic molecule, 1,5-diamino-2-methylpentane, into these junctions alters the I-V characteristics, with the potential to elicit diode-like behaviour forming the basis of nano-scale logic circuits. Previous research has proven the potential of using organic molecules to observe this behaviour [4]. The key to obtaining diode-like behaviour is to have an asymmetry in the charge distribution within the molecule, which can either be achieved through the use of different electrode metals or a physically asymmetric molecule. This report adopts the latter approach for its greater practicality.

1.2 Background

Molecular scale electronics is the branch of nanotechnology focusing on the use of small numbers of molecules. Its roots trace back to the late 1950s following the miniaturization of electronic components like the transistor, invented in 1947 [5] by John Bardeen, Walter Brattain, and William Shockley at Bell Labs. The transistor was created as an alternative to bulky vacuum tube transistors providing a low-power, reliable, and efficient alternative.

Since the 1950s electronic devices have become smaller and faster inline with Moore's Law (see Figure 1); a trend that states that the number of transistors on an integrated circuit of a fixed size doubles every two years. This has been made thanks to the use of silicon electronics, overtaking germanium in the 1960s [6]. Silicon integrated circuits have since dominated the electronics industry following a progression of minimization: "vacuum tube $\rightarrow$ discrete transistor $\rightarrow$ integrated circuit $\rightarrow$ molecular electronic devices." [7]. Despite the natural progression towards molecular electronic devices in the 1980s, the focus remained on silicon-based semiconductor technology due to its well-established design and manufacturing techniques. However, we are beginning to reach technical and physical limits in silicon-based circuits both technically and fundamentally. The current limits of micro-electronic devices can be generally split into physical limits and technical limits. Organic molecules hold the potential to resolve both of these.

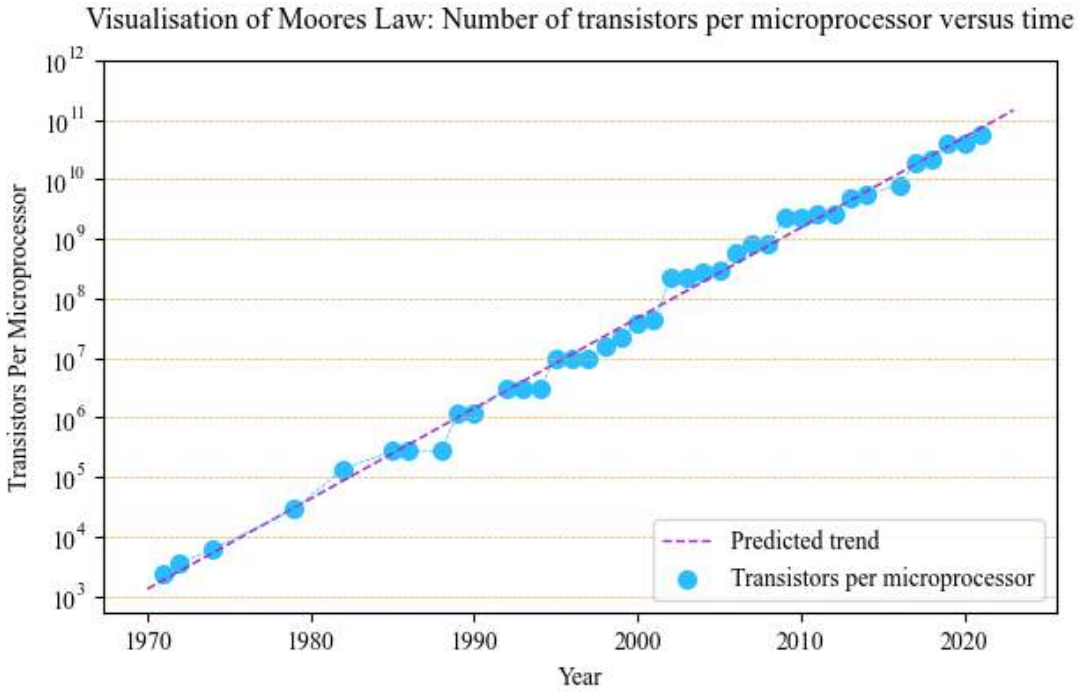

Figure 1: Moore's Law, data taken from: Our World in Data [8]

The miniaturization of silicon-based electronics has brought about many accompanying issues. Regarding physical limits; at nanometer scale devices quantum phenomena are increasingly important for nanometer-scale devices. These lead to leakage currents and increased power consumption. For instance, when the channel region of a transistor is very small, the electric field across the channel becomes very strong, leading to atypical changes in device behaviour including tunnelling and band edge effects. Short-channel effects in Metal-Oxide-Semiconductor Field-Effect Transistor's cause a reduction in threshold voltage making the device susceptible to noise [9].

Regarding technical limits, manufacturing tolerances become very tight when working on nanoscale structures such that lithography techniques have to be incredibly precise - an issue

that is inherently overcome by organic molecules. Other problems that can arise in nano-electronic devices are associated with dopants, a type of impurity intentioanlly added to semiconductor materials to alter their electronic properties. Yet, in small devices, the random distribution of dopants can lead to statistical fluctuations that affect device performance.

Given these challenges, exploration is necessary for alternatives to the 'top-down' construction methods used for conventional electronic devices. Figure 2 summarises the progression of 'top-down' to 'bottom-up', illustrating the fundamental differences between the approaches[10]. It can be seen from this figure the differences in scale between different approaches. This report explores the creation of devices most akin to the Molecular tunnelling FET.

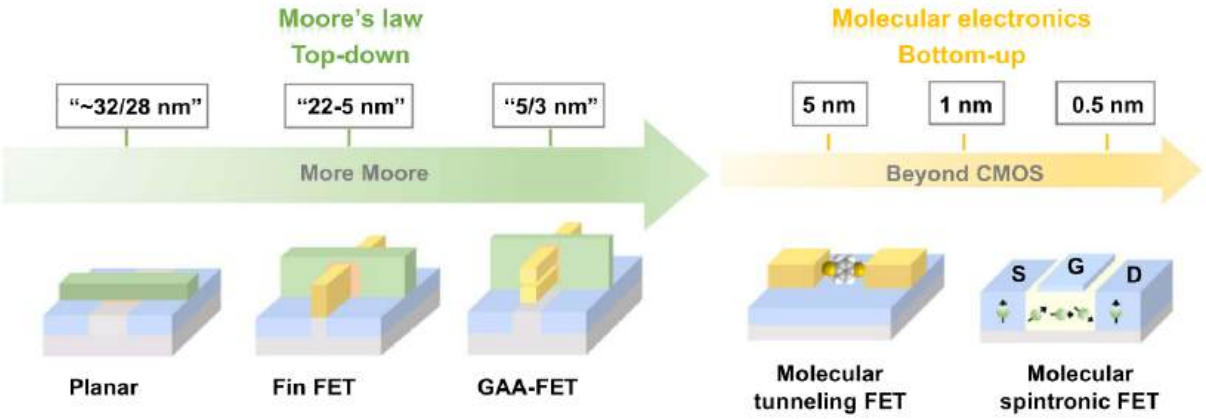

Figure 2: Molecular electronics, a potential candidate for 'Beyond CMOS'. [10]

1.3 Motivation

Molecular electronics thus offers several potential advantages to silicon-based devices, including the ability to fabricate devices at a smaller scale, the ability to precisely control the electronic properties of individual molecules, and the potential to overcome some of the limitations of conventional electronic devices. The size of molecules is usually sub-3 nm and as such shows promise in revolutionizing device miniaturization [10]. Furthermore, organic molecules can be synthesised in large quantities with exact structures removing any potential tolerance issues.

The difficulty of fabricating and integrating individual molecular devices into a functional circuit, however, must be overcome. Taking a 'bottom-up' approach the formation of the connection between the electrode junction and the inserted molecule is the key scientific issue within molecular electronic devices. The stable 'electrode-molecule-electrode' junction, or molecular junction, [10] must be reliably made. This requires reliable contact between the metal electrode atoms and the organic molecules. Hence, precise control over the placement and orientation of the molecules is critical to achieving the desired electronic properties and device performance. The method attempted in this project applies a voltage to the electrodes upon the addition of organic molecules to promote their alignment. Previous work

has utilized multiple organic molecules to 'bridge' the nanogaps. This altered the electronic characteristics of the device yet failed to provide diode-like characteristics consistently.

Another challenge with molecular devices is their stability and reliability. Molecular junctions can be sensitive to environmental factors, such as temperature and humidity, which can impact their electronic properties and performance over time.

Overall the multiple difficulties faced with molecular electronic devices, which are more technical than fundamental, are outweighed by the potential benefits.

2 Literature Review

The primary focus of this project was to create nanowires and form nanogaps. 1,5- diaminomethyl pen- tane was selected as the organic molecule, in accordance with the requirement for anchoring groups on the molecule's ends and an asymmetry that has the potential to elicit diode-like characteristics. This focus on testing nanogaps reflects the main complexity of making molecular devices: the integration of molecules into circuits.

Ion-Beam-Induced-Deposition (IBID) was used to form the nanowires, with some minor testing in Electron-Beam-Induced-Deposition (EBID). This was due to both the availability of machines and their potential for desirable nanowire structures. The wires were then broken via electromigration and Joule heating. There are multiple alternative methods to achieve similar outcomes which are discussed in this literature review.

2.1 Molecular Junctions

Molecular junctions can be split into static molecular junctions and dynamic molecular junctions[10]. Typical static molecular junctions are the electromigration junction, Eutectic Gallium-Indium (EGaIn) junction and Carbon-based junction. Typical dynamic molecular junctions are the Scanning Tunneling Microscope Break-Junction (STM-BJ), Mechanically Controlled Break Junction (MCBJ), and Micro-Electromechanical-System Break-Junction (MEMS-BJ).

The electromigration junction (see Figure 3) is the focus of this project. It is a type of static molecular junction where although the distance between electrodes can not be directly controlled the break size can be influenced under appropriate failure conditions. This technique involves the failure of wires under current stress. Thin wires ($< 1\mu m$) can be failed by the process of electromigration, from the thermally assisted motion of ions under the influence of an electric field. This process can be done under ambient conditions, is highly repeatable and can be conducted on multiple local wires. Further details of this method are discussed in Section 2.2.

The EGaIn junction is formed from a moldable liquid metal with non-Newtonian properties.

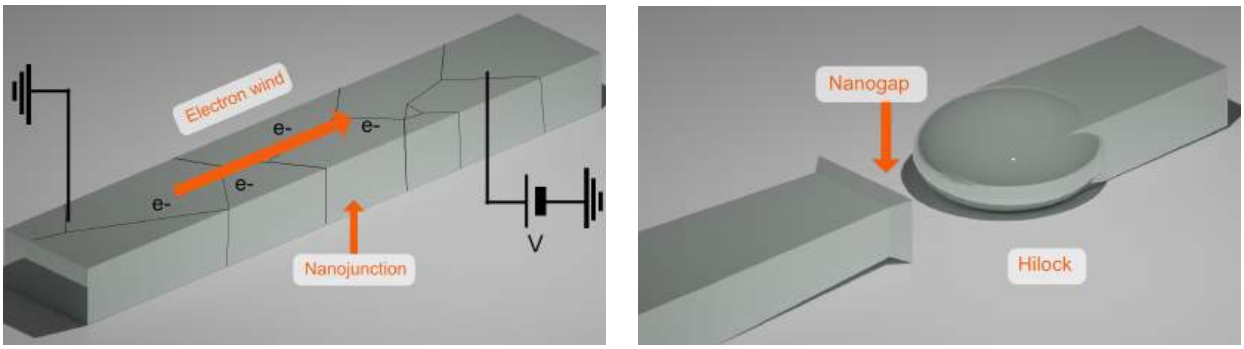

(a) Electromigration in nanowire **(b)** Post breakage

Figure 3: Diagramatic process of electromigration to form nanogaps in metal wires

The metal is a liquid at room temperature but does reflow to form the shape with the "lowest interfacial free energy as do liquids such as Hg and H_2O "[11] .This means it can form metastable structures, specifically conical tips that can be brought into contact with a self-assembled monolayer (SAM). The EGaIn tip electrode in contact with a SAM on a substrate, serving as the bottom electrode, forms a metal-molecule-metal junction. However, the shape of these junctions makes them unviable for this project: the tip is around $1\mu m$ in size and forms a layered junction.

Carbon-based molecular junctions are a type of static molecular junction that utilizes carbon-based molecules as the active component. For instance, nitro-azobenzene oligomers (2-5nm) bridge a gap between two electrodes providing non-linear tunnelling characteristics [12]. The main transport mode is quantum mechanical tunnelling, similar to the electromigration junction. Carbon-based molecular junctions can be fabricated using a variety of techniques, including self-assembly, chemical vapor deposition, and scanning probe microscopy. These devices potentially offer advantages over traditional semiconductor-based devices, such as high scalability, low power consumption, and the ability to operate at room temperature. However, they are sensitive to environmental factors over time, suffer from high contact resistance between molecules and the electrodes, and can be challenging to interface with traditional electronic components.

Dynamic molecular junctions can be repeatedly opened and closed, exemplified by the STM-BJ. In this method, the nanogap is formed between the metallic STM tip and the metallic substrate, with a thin layer of molecules deposited on the metallic substrate. The STM tip is then pushed into the substrate surface and slowly retracted. A metal-metal atomic junction forms. If a molecule is bonded to both metallic contacts then upon further retraction a metal-molecule-metal junction can form. Whilst this forms the basis of the molecular device, it is not scalable for logic circuits.

The MCBJ is another dynamic molecular junction. In this technique, a metal wire is drawn until it breaks, creating a small gap that can be bridged by a small number of molecules (or even just one). The distance between the two ends of the broken wire can be precisely controlled, enabling the electrical conductance of the molecule to be measured as the wire is stretched.

The nanocontacts are fabricated on a flexible substrate, which is then bent to stress the wire. An attenuation factor relates the electrode displacement and bending of the substrate [13]. This method often uses lithographic techniques and bending of the substrate. Thus this technique is undesirable as it cannot be scaled and enables only one device per sample.

2.2 Nanogap formation via Electromigration

The principal method used in this project is the fabrication of molecular junctions via electromigration. Although research towards this has previously been conducted, the combination with FIB fabricated wires promises new insight regarding nanowire fabrication and design.

When a wire is electrically stressed the mobility of the metal ions increases ([14]). Electromigration is a process whereby ions in conventional current-carrying wires move against the direction of current flow, causing wire failure over time. The motion of these ions is caused by the "electron wind" created when a wire is electrically stressed, resulting in increased heating and the movement of metal atoms. The theory for bulk materials links mass transport directly to a functio of current density and can be categorized by the "mean time to failure" (MTF). This theory is demonstrated in equation 1.

$$MTF = AJ^{-n}e^{(\phi/kT)} \tag{1}$$

- A constant relating to cross-section
- J current density, Acm^{-2}
- ϕ activation energy , Ev
- k Boltzman's constant
- T film temperature, K

Durkan and Welland have proposed a considerably faster alternative technique to MTF [15], which is considerably faster. The idea is to ramp up the current density in a time much shorter than the MTF, allowing for the determination of a failure current density that can be used to assess the durability of interconnect designs. If the rate of current increase is slower than 1/MTF, and the stress is only growing slowly with time, then this method can give valuable information on trends.

Whilst the structure of nanowires formed via FIB deposition was found to be amorphous, Durkan and Welland's prior research helped to guide potential testing and analysis of nanowires in this project. It was observed that for thin wires (sub 100nm) the failure of the wire is towards the middle of the wire. For these wires, breakages were dominated by Joule heating and thermal stresses driving grain restructuring. The temperature profile in thin wires

means grain growth is largest at the centre, imposing the largest stress on this location to give breakages in the middle. The closing remark suggests best performance is observed by fabricating wires on very thin oxide layers and with short wires.

Hadeed and Durkan conducted further tests on the fabrication of nanogaps via electromigration in gold and gold-palladium wires [16]. 50nm wires were stressed to create nanogaps through electromigration and thermomechanical stress. They found that to achieve nanogaps of 1-2nm size voltage ramping was more effective than current ramping as the current is self-limiting this way. Applying the current ramp had a high potential to cause irreversible damage to the samples. The failure of wires is primarily determined by the current density J_{fail}. It was also found a rate of increase of $4mV/s$ observed clean-breaking $I(V)$ characteristics.

2.3 IBID for nanowire formation

IBID mechanisms offer insight into the behaviour observed in the project. Trimethyl (methylcyclopentadienyl) platinum was used as the precursor.

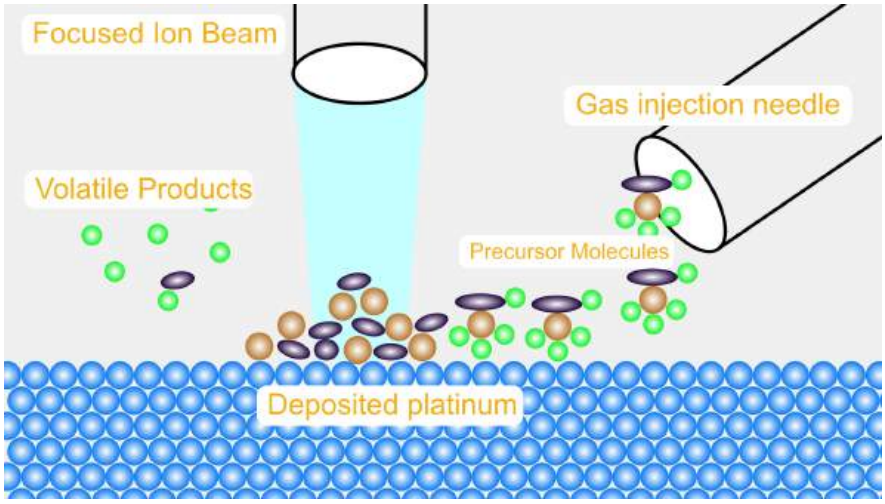

Figure 4: Focused ion beam deposition

The general process observed with precursor gases starts with bleeding the precursor into the vacuum chamber via a needle set within $100\mu m$ of the surface of the specimen. The precursor then adsorbs to the substrate surface. Precursor molecules are broken down by both the ion beam and secondary electrons produced from ion-atom interactions. The volatile products are then pumped out of the system along with any gaseous precursor molecules that did not adsorb to the surface, such that growth is only observed in the targeted region, over which the ion beam is scanned. This is shown in Figure 4.

Both FIB systems used in this report used the precursor gas trimethyl (methylcyclopentadienyl) platinum (see Figure 5), henceforth referred to as the "platinum precursor." How this is decomposed and what microstructure results are essential to analyse the nanowires and

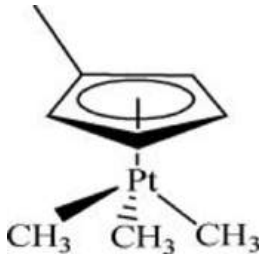

Figure 5: trimethyl (methylcyclopentadienyl) platinum [17]

nanogaps in this project. The two main mechanisms behind this precursor decomposition are dissociative electron attachment and dissociative ionization [18]. While these proposed mechanisms assume nanowire formation via Focused-Electron-Beam-Induced-Deposition, same as EBID, the similar production of backscattered electrons and ionization capabilities of FIBID make the decomposition mechanism noteworthy. Dissociative electron attachment causes rupture of a $Pt - CH_3$ bond, forming the negative ion fragment $[MeCpPtMe_2]^-$. Dissociative ionization can rupture two or three of these bonds, forming $[MeCpPtMeH]^-$ and $[MeCpPtCH_2]^-$. It was observed that the formation of bare Pt^- from dissociative electron attachment and Pt^+ from dissociative ionization was only a minor channel and partial decomposition is much more common.

Although Pt can also be deposited via EBID, this is reported to produce wires with higher resistivities. The mechanism of decomposition is very similar to that of FIBID, varying in the ratios of different breakdown mechanisms.

The resulting microstructure of the deposited Pt is discussed in [19]. It is reported that after $PtCH_3$ bond cleavage, the compound is decomposed to form a reduction of platinum atoms/clusters embedded in an amorphous carbon matrix. A diagram of this reported breakdown is presented in Figure 6. Unfortunately, carbon is heavily incorporated in the deposition and growth process, forming a "dirty" metal. The measured composition of wires deposited with 15keV electron beam deposition, using $MeCpPt(Me)_3$, have been reported as 21.5% Pt, 73% C, 5.5% by mass. A Gallium ion beam at 30keV gave 45% Pt, 45%C, 5% Ga, 5% O, at 35keV gave 46% Ga, 24% C, 28% Ga and 2% O, and at 25keV gave 13-21.5% Pt. These large differences affect the microstructure during electromigration however the recorded resistivities range from 70-140$\mu\Omega cm$. [20].

In addition to the deposition by the Secondary Electrons (SE) the scattered electrons and ions result in the deposition of Pt. These can scatter at angles away from the pattern and result in a halo around the wires (discussed in Section 5). Utke, Hoffman and Melngailis reinforce the use of FIBID against FEBID to produce wires with a greater Pt: C ratio. This did, however, come with a larger 'halo' of deposition around the patterned site. The conductivity of this halo is generally very low but depends on the wire composition.

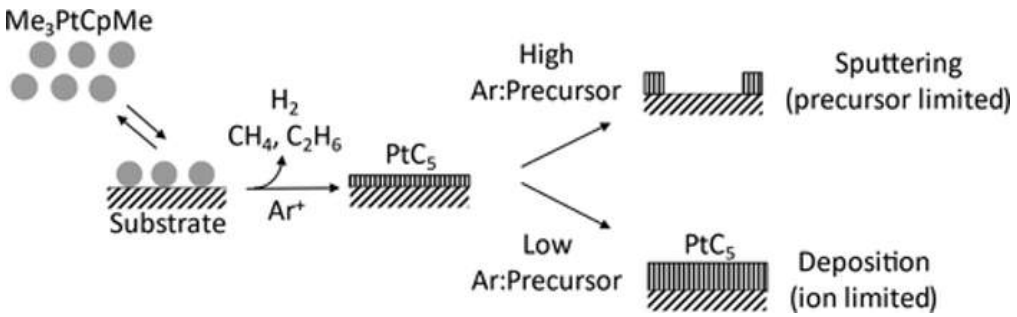

Figure 6: trimethyl (methylcyclopentadienyl) platinum breakdown mechanism, using an argon ion beam [19]

3 Theory and Design of Experiment

The project explores the fabrication of nanoscale interconnects via various methods. First is Ion-Beam-Induced-Deposition (IBID), followed by the deposition of organic molecules with specific linkers to allow them to attach to the wire material into nanojunctions in these wires. Current is then measured against voltage at various temperatures on these devices to elucidate the main mechanisms behind conduction in these molecules. A simplified diagram of a potential structure is shown in Figure 7. Multiple molecules are expected to line-up in parallel or series to cross the formed nanogaps.

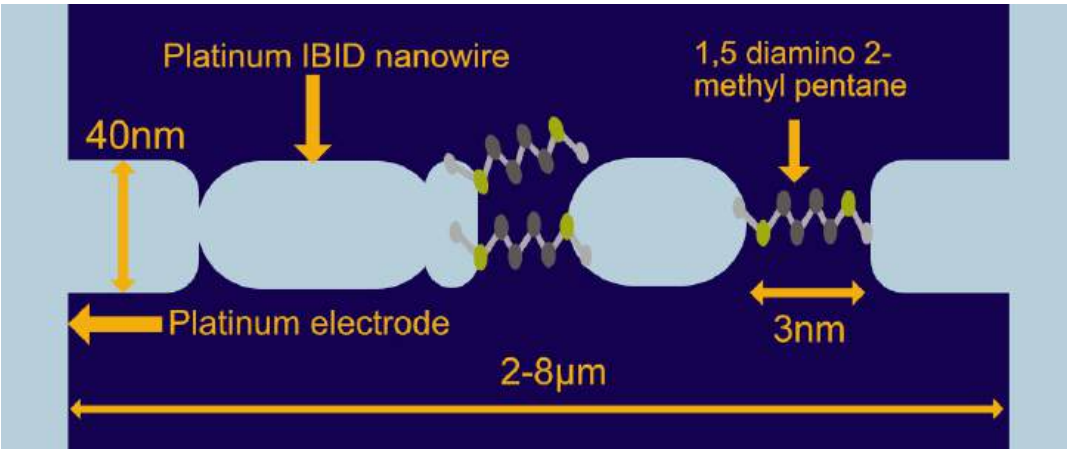

Figure 7: Diagram of potential molecular device

For this goal, it is desirable to create wires of various lengths with sub-50 nm widths and thicknesses. This is because thinner nanowires fail more reliably and consistently to form nanogaps of the desired size (1-2nm) [16], whereas wider wires fail subject to the effect of the wire's microstructure. Although nanogaps of 1-3nm are most desirable, electromigration has some variability to it.

The project evolved throughout the year. It initially focused on using the Zeiss Orion NanoFab machine in the nanoscience centre – a Gas Field Ion Source (GFIS) Focused Ion Beam (FIB) system. It consists of a helium-neon ion column and a galium ion beam column offset by 54°. The microscope is further fitted with an OmniGIS II and an Omni insitu

probe (see Section 4 for more detail). The helium-ion is preferable to traditional E-beam lithography for its potential capability to fabricate intricate wires of widths 10-50nm without the need for a photoresist. The capability to image, mill and deposit together allows a larger amount of flexibility in operation. Helium-ion beams have smaller 'halos' than traditional FIB methods and as such are very suitable for our application. EBID was also attempted in small amounts as an exploration.

Partway into the project the Helios Nanolab system was also used, equipped with a Gallium FIB and Scanning Electron Microscope (SEM). This was used for various reasons, partly due to unforeseen complications with the Orion system as detailed in Section 4.5. Results from these two microscopes were then compared and contrasted. In addition to ion deposition limited experiments, electron beam deposition tests were also undertaken.

The initial aims and objectives of the project were to:

- Observe the provided samples, consisting of Pt contacts with $2-10\mu m$ gaps, using the Helium FIB.
- Fabricate a variety of nanowires using IBID.
- Image a set of wires to determine their topology and efficacy of fabrication.
- Observe the electrical characteristics of IBID nanowires.
- Form nanogaps in said wires through voltage ramps and electromigration.
- Image a set of nanogaps to determine their formation.
- Test insertion of organic molecules into formed nanogaps.
- Observe any changes to I(V) characteristics.

4 Apparatus and Experimental Design

The systems used for this project were all located at the Nanoscience Centre and Cavendish Laboratory on the West Cambridge Site.

4.1 Test chips

Four separate platinum electrode test chips were used for the project (Ossila, product S403A1), detailed in Figure 8. Whilst these chips are designed for OFET testing with a bottom-gate bottom-contact architecture, this project used them simply as electrode contacts. The chips consist of a highly P-Doped (boron) silicon wafer coated with a 300-nm layers of SiO_2 on each side. The platinum contacts are made from a 5nm titanium adhesion layer with 100nm of

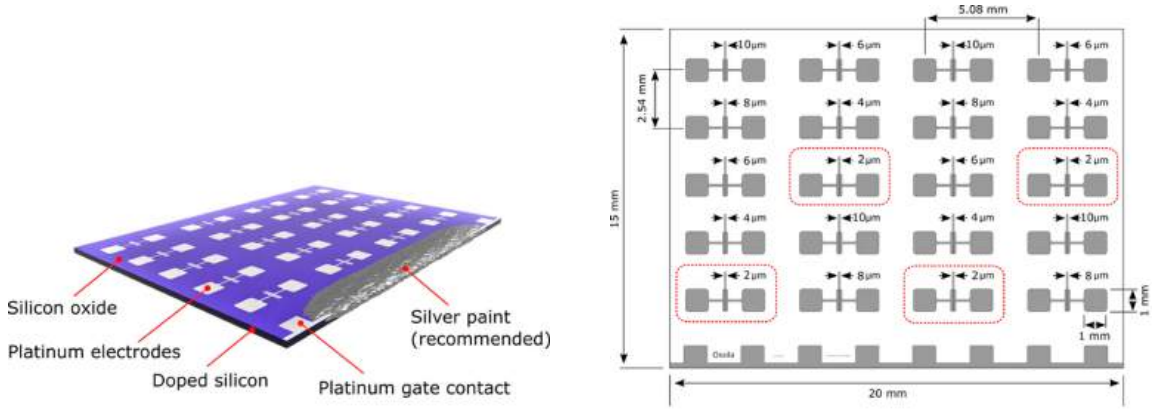

(a) Platinum OFET **(b)** Ossila platinum test chips

Figure 8: Images of test chips [21]

platinum deposited on top. The platinum gate contacts at the bottom were left untouched; voltages were simply applied between platinum electrodes during testing. The nanowires were fabricated in the spacings between the electrodes ranging from $2 - 10\mu m$. [21].

20 sets of electrodes are present on each chip, providing 80 potential nanowire fabrication sites with many of these tested throughout the project. The benefit of a silicon dioxide substrate is that it is both a great electrical and thermal insulator, meaning that no leakage current should come from the chips. However, any rapid thermal fluctuations in the nanowires may cause large stresses between them and the substrate.

4.2 Helium, Neon Focused Ion Beam

A large part of the project in the first term involved operating the Zeiss Orion NanoFab machine located in the Nanoscience Centre (see Figure 9). Previous work used electron beam lithography to create the nanowire structures, however using this machine wires could be fabricated via exposure of a gaseous platinum compound to helium ions.

The use of this machine required learning how to operate the NanoFab machine in all capacities along with subsidiary parts like the Gas Injection System (GIS). Details of its operation are provided in Section 4.2.1 and are relevant for subsequent data analysis. The operation of a FIB starts with the insertion of a gas (helium or neon for instance) which is ionised in the gun portion of the column. A positive voltage at the source (around 25 kV) and a negative voltage at the extractor (around -30 kV) create a strong electric field that ionizes gas atoms as they approach the tip of the gun. The tip of the gun is made of a tungsten trimer, a 3-atom tip that determines the point of ionization of the gas, typically lasting a couple of weeks when used for solely imaging with helium. The ionized gas then flows towards the extractor and forms into a beam. This beam is condensed via voltage-controlled lenses and shifted/tilted via quadrupoles and octupoles, around 10-20 kV. The beam interacts with the sample through collision cascades producing ions and electrons from the sample. These

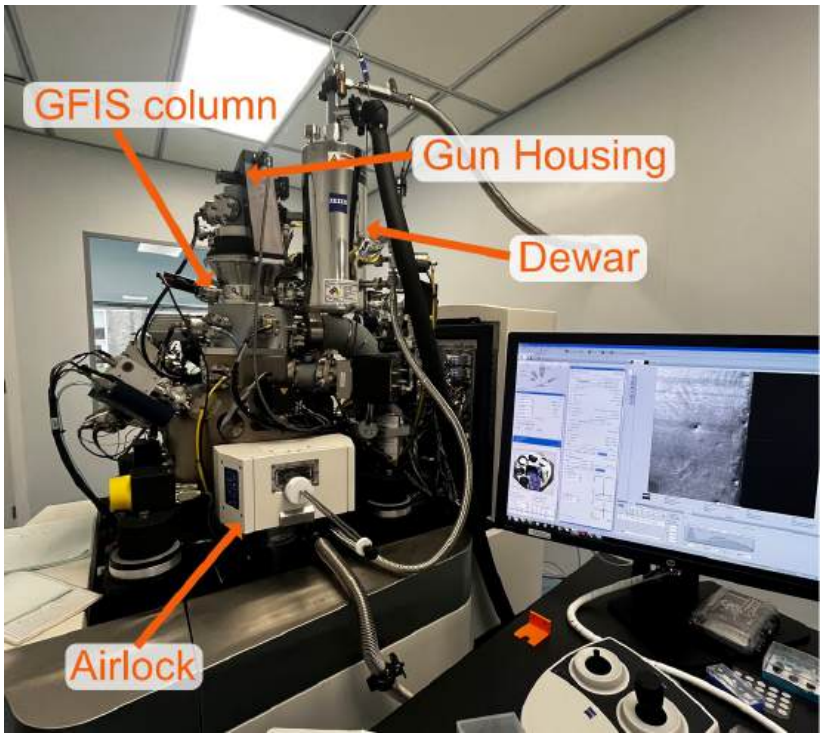

Figure 9: Zeiss Orion Nanofab machine -West Cambridge

secondary electrons are collected by the Everhart-Thornley Detector (ETD) as the beam is scanned. These electrons create a small electrical signal that is amplified to provide images, as seen throughout this report.

Helium-ion Microscopy (HIM) produces images with a higher resolution than low kV electron microscopy as a result of the smaller spot size (less than 0.3nm at energies of 25-30kV). Only secondary electrons from the surface can escape to the ETD giving a clear overall image. [22]

The mechanisms which govern the ion-solid interactions are complex and extensive. Figure 10 illustrates the reported mechanisms of these interactions for a series of ion beams, including secondary electron emission (1), polymerization (2), secondary ion emission from nuclear interactions (3), dislocations and vacancy formation (4), interstitials (5), phonons (6), backscattered ions (7) and ion implantation (8) [23].

HIM benefits from a very small final probe size since helium ions have a de Broglie wavelength of $\lambda = 0.08pm$, removing limitations of diffraction. The helium ions then neutralize in the first few nm of the sample and the resulting positive charge at the surface can be neutralized by a low-energy flood gun, pre-installed into the system.

The He beam is used on the tool, but the gas can also be switched to Ne. The neon ion capabilities with the Zeiss Orion nanofab make it suitable for structures over 20nm in size, which were tested for this project. The neon beam has a slightly higher sputtering yield than helium placing it in between helium-ion beams and gallium-ion beams in terms of operational scale.

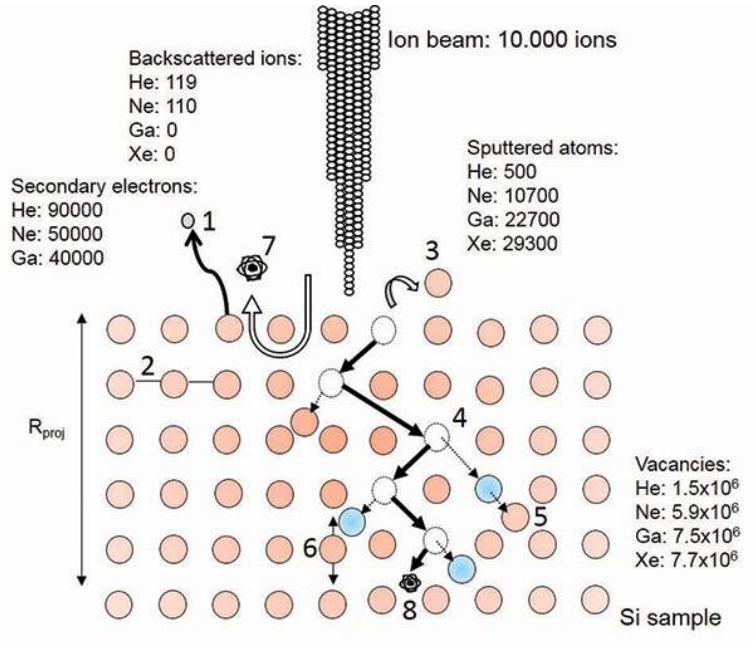

Figure 10: Diagram of Ion interactions with a Silicon sample [23]

4.2.1 Helium, Neon FIB operation and experimental design

Once the samples had been collected and briefly imaged under the light microscope they were placed inside the nanofab chamber to be imaged. A large portion of the beginning of the project was spent learning the operation of the relatively new nanofab system. Regarding sample preparation, the samples came covered with tape from the manufacturing process which was removed. The sample was then placed on a specimen stub using a conductive carbon disc and screwed into the specimen holder (see Figure 11). As the samples were desired to work under room temperature and pressure no other sample preparation was needed. The loading process into the Nanofab chamber required insertion into the airlock and then a transfer sequence via the system software/airlock panel controls.

The system was then initialized and continually monitored for various parameters. These can be seen in Figure 12 and include:

- Chamber and gun pressures
- Extractor and accelerator voltages
- Lens voltages
- Probe current, landing energy, aperture
- Dewar temperatures and pressures

The extractor potential is the voltage corresponding to the tungsten tip. The accelerator voltage increases the speed of ions to their final energy. The beam focus is determined by

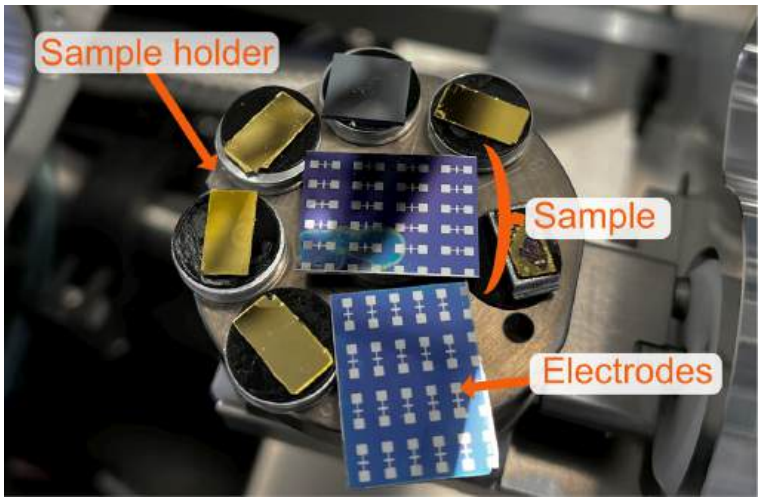

Figure 11: OFET chip prepared on sample holder

voltage control of two lenses, in combination with quadrupoles. Lens 1 condenses the ion beam before the aperture, whilst the voltage of Lens 2 determines the focus point. The Dewar cools liquid nitrogen to a 'slush' of 57.3 K. This keeps the tungsten tip and trimer at its operating temperature of 77K.

Once the sample was loaded into the nanofab chamber it was positioned to the eucentric position height. The eucentric position was such that the specimen remained at constant height during tilting operations and hence did not collide with the GIS probe. The eucentric height corresponded to a working distance of 8.4 mm, or stage height of around 3.8mm. (usually 8.5-9.0mm, however the sample was relatively thick). The individual electrodes were then imaged using the helium beam.

Parameters needed continual adjustment throughout this process, from varying sample heights to imaging at different angles. Figure 13 shows the diagram of the system status from which key operations could be controlled. These included starting the gas flow to increase the GFIS column pressure (a change also observed in the GFIS column and GFIS gas box tabs on the side) and initiating the transfer sequence. It was important that all pressures operated within the thresholds and that these were visually checked upon system startup (see the Manual for a detailed list of the start-up sequence).

4.2.2 Gas Injection System operation

The Gas Injection System (GIS) was used in conjunction with the FIB to deposit platinum. The Orion Nanofab system was fitted with the Oxford Instruments OmniGIS II gas delivery system. Three cartridges are stored on the machine containing different precursor gases. For this project a platinum precursor was broken down to deposit platinum wires. This precursor gas was selected as it operates under the largest range of beam parameters and is therefore suitable for the majority of metal deposition scenarios. Although the alternative, tungsten

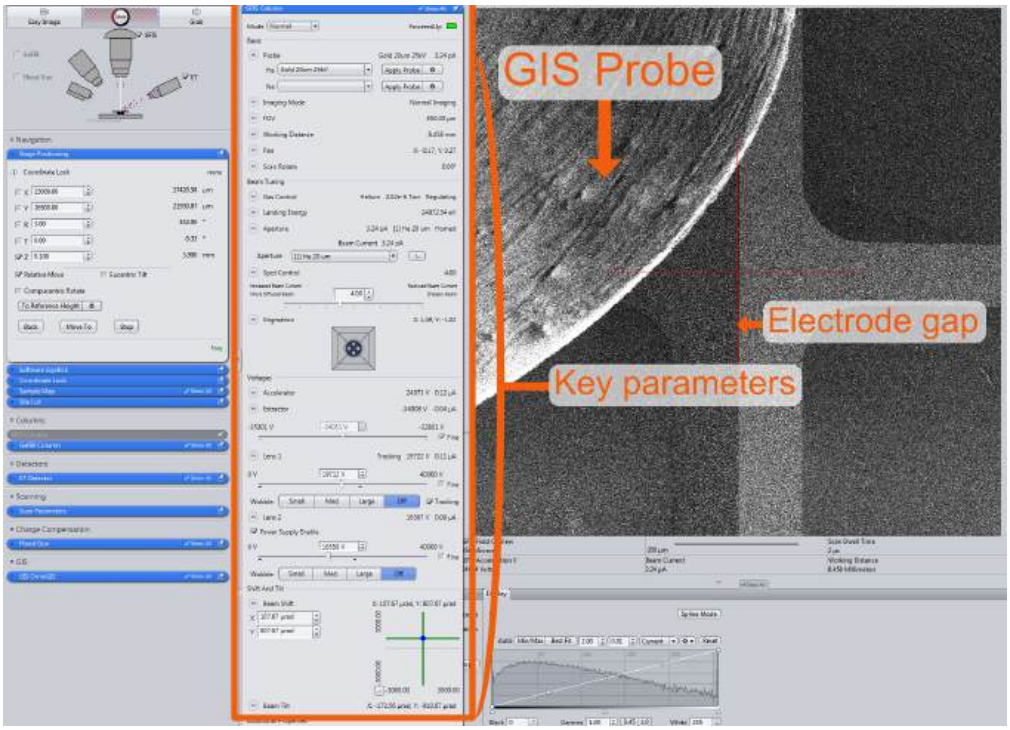

Figure 12: Orion system setup

hexacarbonyl, $W(CO)_6$, has a higher conductivity than platinum, it is difficult to use at it can block the GIS needle.

Since the OmniGIS is made independently of the Orion Nanofab machine and software extra precautions had to be taken during its operation. For the probe to be effectively used the sample must be positioned at the eucentric position position in the chamber. This reduced the concern of scratching the specimen when moving between electrodes and tilting the sample. On first use, the sample should be moved down to ensure the pre-set inserted position of the GIS needle does not touch the specimen.

After this, the 'inserted' position of the probe was set in the system software. The probe was then positioned to be 100 microns above the surface of the specimen, achieved by moving the needle down until it contacts the specimen and then moving the needle upwards. The separation of the needle and substrate impacts the local flux: too small a separation and the precursor does not adsorb to the whole area that is being scanned; whilst too large a separation and the gas is not sufficiently replenished to deposit platinum.

Since the FIB can also mill away at the surface of the electrodes, the positioning of the needle is critical to the performance of the system and often required multiple attempts/ revisions. The insertion of the needle shifts the image created by the ETD which must be accounted for when patterning with the Orion software. This is a result of it being grounded which bends the trajectory of generated secondary electrons as they are drawn to the ETD.

Once positioned correctly the patterned line was drawn and parameters were set in the Orion

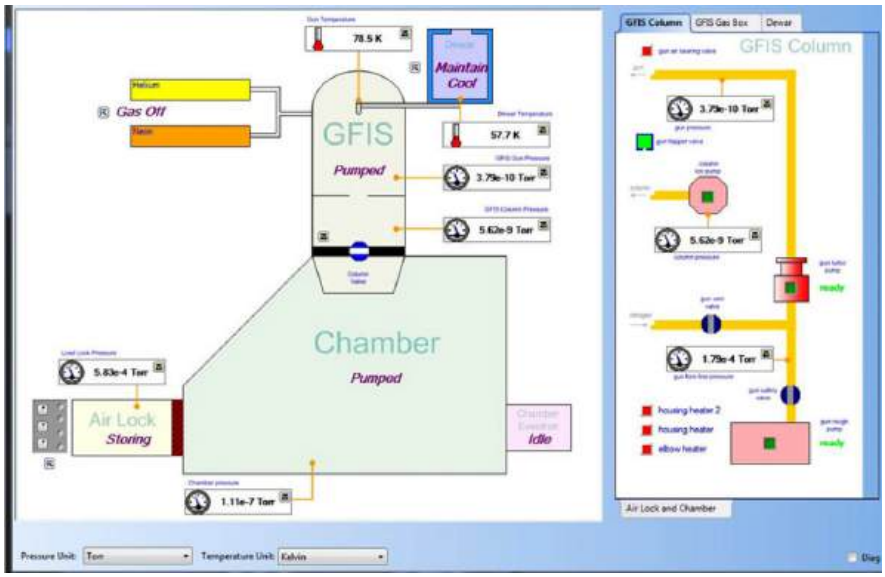

Figure 13: Orion System Status Screenshot

software. The imaging mode was changed from continuous to 'photo grab' to capture the specimen. The platinum precursor was heated to its operating temperature of $45.0C$, and then set to flow out of the nozzle at $54.0C$. This heating ensured that the precursor was in a gaseous state. The system used feedback to bring the gas flow up to a target pressure of $1.00E-5$ torr, yet as seen in Section 4.5 several issues became apparent with this system.

After deposition the gas flow was stopped, the needle retracted and time was left for the gas to be pumped from the chamber. This prevented Pt deposition from imaging. The whole process took around 20 minutes per sample, including waiting for the chamber returned to its target pressure of $2E-7$ Torr.

This process was repeated for each nanowire constructed for varying sizes and shapes. Multiple designs were tested throughout the project, with detail provided in Section 5. All gap sizes were tested from $2\mu m - 10\mu m$. Line widths varied from sub 50nm to 100nm, with varying success.

4.3 Gallium Focused Ion Beam

The gallium ion beam on the Helios Nnaolab system was used predominantly in the latter half of the project (see Figure 14) due to the Orion system being in an unusable state for several weeks. The Helios system was still very capable of fabrication of sub-100 nm wide nanowires.

Gallium ions interact with different characteristics (particualrly surface damage and penetration depth) to neon or helium ions, which were considered during the project. The FEI Helios Nanolab benefits from an included SEM. The Ga ions being heavier than He and Ne means the beam has a much higher sputtering rate causing damage to the surrounding surface

and potentially larger and 'dirtier' wires. The Helios GIS system used the same platinum precursor.

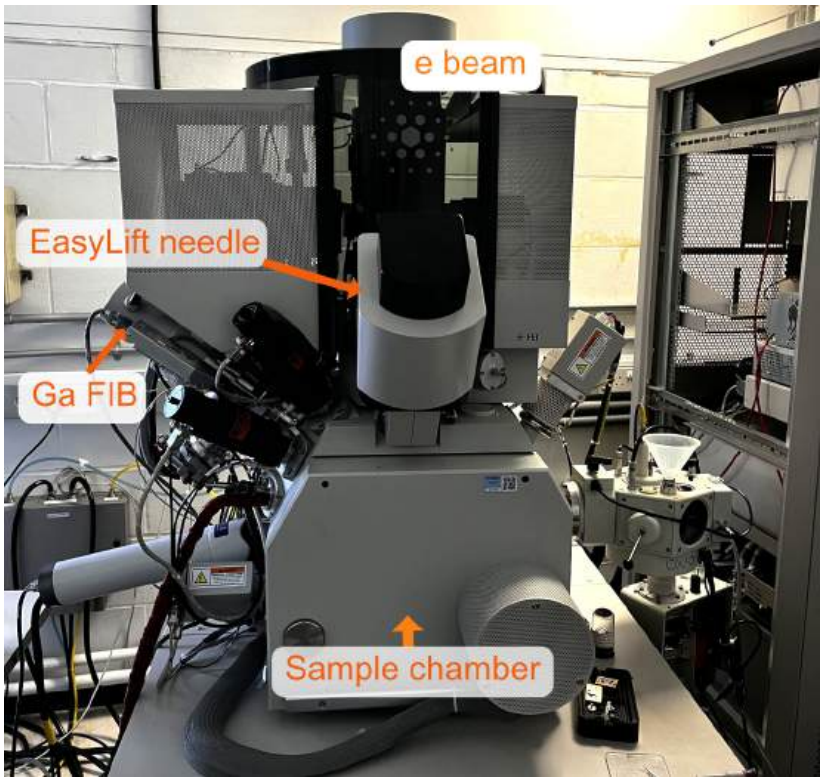

Figure 14: Helios setup - Cavendish Laboratory

Whilst the Helios system shared many similarities with the Orion system, its operation differed in some significant ways. Sample preparation remained unchanged.

Many of the same parameters were used for the FIB and corresponding SEM. The sample was moved to the eucentric height and both the Ga FIB and SEM were aligned. The GIS probe was then inserted and precursor gas was heated. The GIS probe was integrated into the system software making use much simpler and more efficient. Predicted deposition rates and material heights were given to the user making parameter estimation a simpler process. After the selected target space was set on the software the deposition process was started to form nanowires of, again various lengths and heights. An example of the system software is shown in Figure 15.

4.4 Probe-station

To form the nanogaps in the wire, voltage ramps were induced using a high-precision source meter. This enabled very controlled voltage ramps of 1-4mV/s to help obtain the target 1-2nm gaps. Figure 16 shows the setup present in the nanoscience centre.

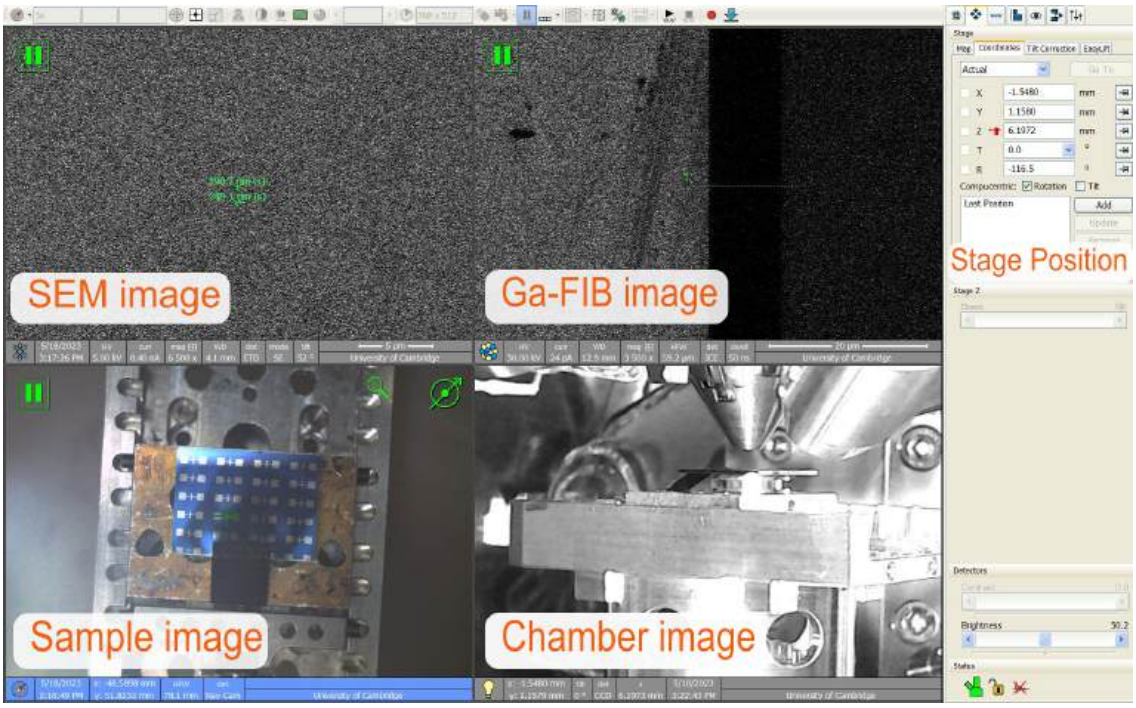

Figure 15: Screengrab of Helios software

4.4.1 Nanowire characterization process

A Keithley 2450 source meter was used to provide the voltage ramp. The current was passed through metal needles which were positioned using Quater Research micropositioners. These were carefully placed onto each set of electrodes, with the help of a Brunel Microscopes light microscope as shown in Figure 17. Each sample was then given a test of voltage ramps going up gently from 100mV to 2V. Two alternative methods were used to provide these voltage ramps. Keithley Kickstart software was used first, allowing remote control of the Source Measurement Unit from the computer where plots could be saved directly to a USB. The license for this software ended during the project and so for the remaining voltage tests, data was extracted directly from the SMU as Excel files. These were post-processed in Python, enabling the determination of differential plots and average plots.

If very high resistances were observed (order of $G\Omega$), then the voltage was increased due to the high likelihood the nanowire must be annealed to form a proper connection to the electrode. Without this annealing process, the main transport mechanism was dominated by electron tunnelling between the electrodes and the nanowire since the deposited line adhered to the surface. A limit of 20V was set for safety reasons. The success of this process varied.

4.4.2 Nanogap formation process

Wires in which linear characteristics were observed were taken to the next stage. This involved steadily increasing the voltage ramps to very gradually promote nanogap formation

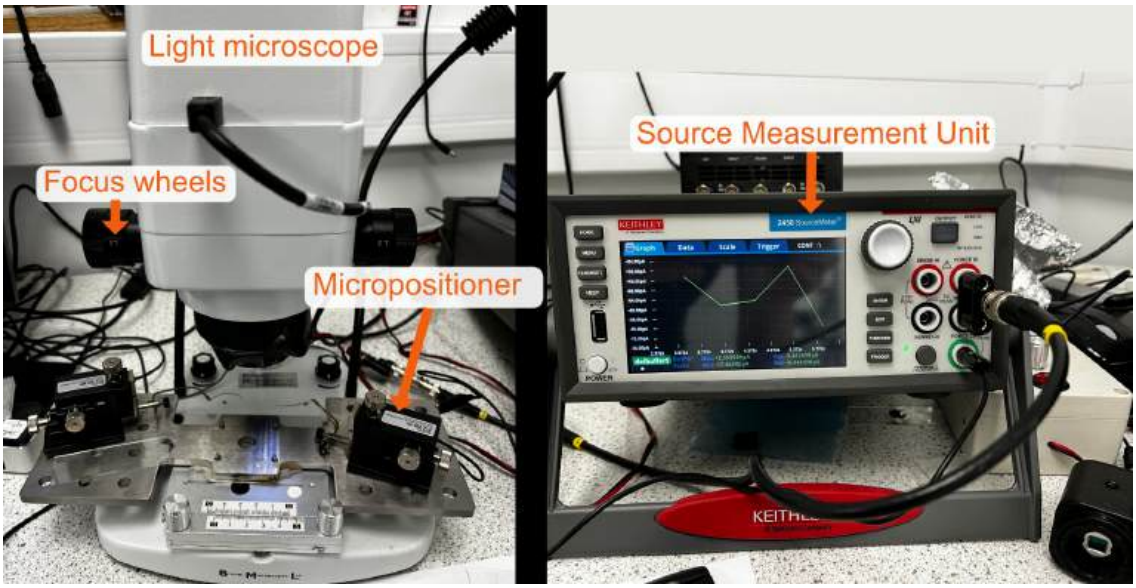

Figure 16: Probe station setup

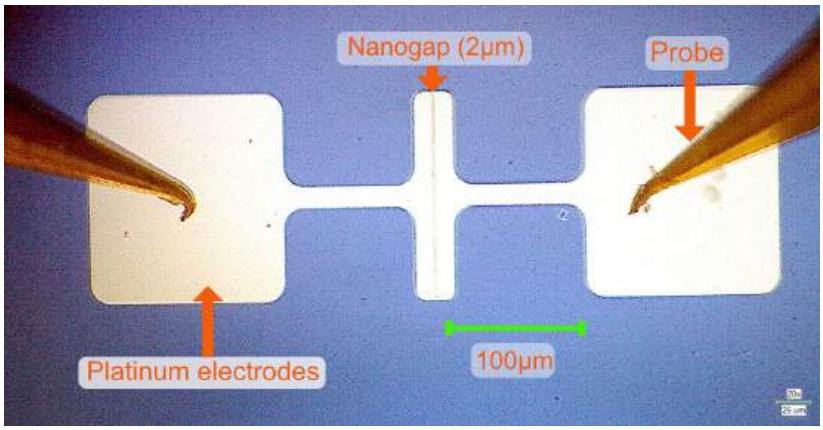

Figure 17: Microscope image of probes and electrodes

via electromigration and Joule heating, illustrated in Figure 18.. A successful nanogap formation started with linear characteristics when ramping to a voltage of around 1.2V. This arose from successful nanowire fabrication and occurred before the nanogap was formed. Thermal effects then began to take over resulting in an increase in resistance. This was followed by inflexion and a drop in resistance until breaking.

4.4.3 Organic Molecule insertion

The organic molecule used for this project was 1,5-diamino-2-methylpentane. A pipette was initially used, however this released too much liquid onto the specimen. A needle was therefore used for the remaining tests. An example of a set of electrodes after the addition of 1,5 diamino-2-methylpentane is shown in Figure 19.

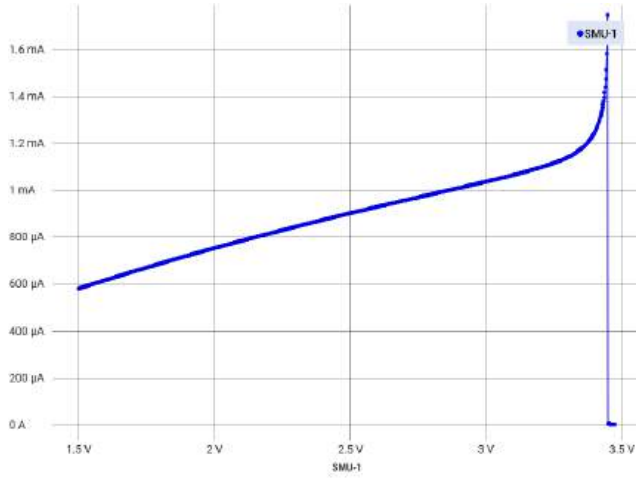

Figure 18: I(V) characteristics when breaking a nanowire

While the liquid was deposited, the Keithley source meter was set to a voltage of 3V to promote the alignment of organic molecules. This was set up using the interface on the Keithley source meter. In some circumstances, an Ossila Source Measurement Unit was used which provided a constant voltage and more effective measurement of the system. A series of voltage sweeps were then run through the specimen as the liquid evaporated. Tests were run in the following days to determine any changes and check stability.

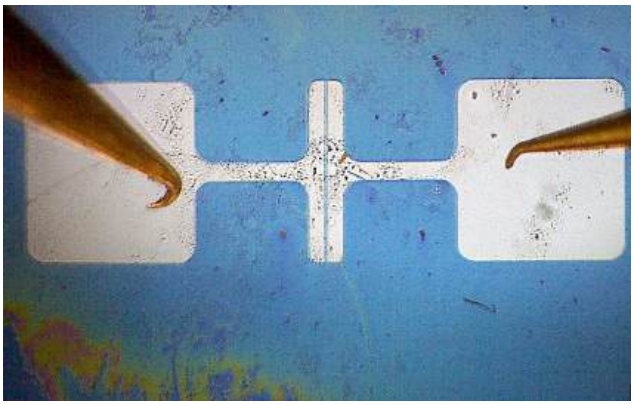

Figure 19: $8\mu m$ sample after the addition of organic molecules

4.5 Experimental inaccuracies and setbacks

There were a series of setbacks throughout the project. Some provided new insight, some were experimentally unavoidable and some were more tedious. Aspects regarding experimental success are detailed in the discussion section. This subsection focuses on overcoming obstacles in the project.

The operation of the Zeiss Orion nanofab system requires consistent maintenance. By nature, the imaging quality degrades over time as the quality of the trimer worsens. This results

from remaining at high voltages for long periods of time, such that collision with the gaseous environment causes one or more of the atoms to break away from the tip of the gun. This requires trimer reforming and re-establishing the Best Imaging Voltage. This process takes several hours of attention and includes pulsing voltages, mechanically aligning the gun, setting the crossover voltage, and determining the beam tilt and beam shift. This must be done every few weeks when using the helium FIB. In combination with compensating for astigmatism and beam focus, this leaves many parameters to be set for the imaging process which change between apertures and ionizing gases. As such, a significant amount of time was spent setting up the FIB to achieve the necessary quality of imaging for pattern deposition.

The OmniGIS probe fitted with the nanofab system had difficulties regulating precursor gas pressure throughout the project. The result was a very slow rise to the target pressure increasing the time between individual wire fabrications. This remained unresolved despite best efforts. The changes in gas pressure resulted in different Pt gas fluxes at the samples, impacting the rate of growth of the wires. In the absence of external input it seems likely that this issue will remain unresolved, exemplified by Figure 20 in which a spike in pressure is visible when the precursor is turned off. A roughly 15-minute period was then needed to bring the chamber pressure to imaging levels, ensuring that no further precursor was deposited by imaging.

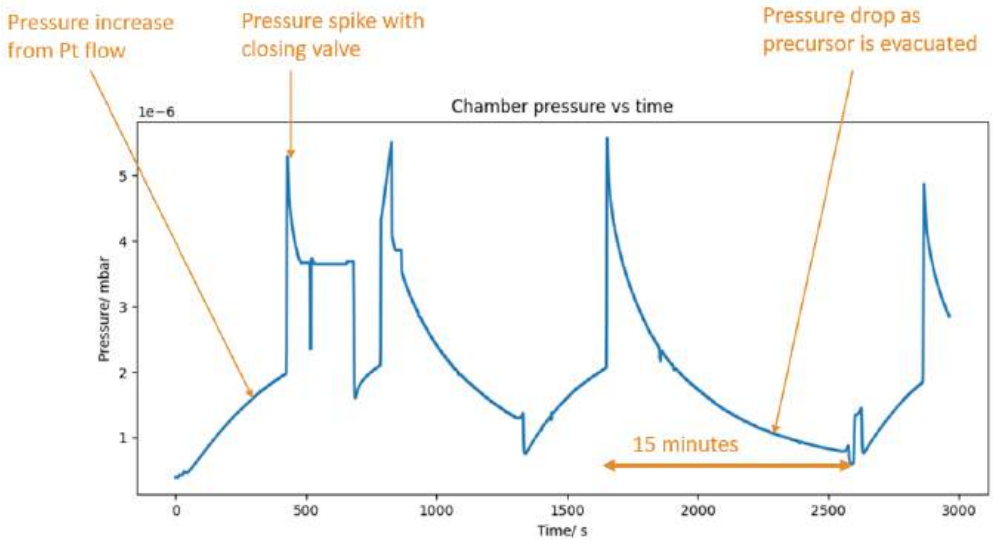

Figure 20: Local pressure around the GIS needle during operation

During the project, the helium gas in the system ran out. Designed to be bled into the pipes and then regulated by hand every few weeks the replenishing of helium was a standard process. However, the change in pressure caused issues with the helium leak/needle valve, resulting in large pressure spikes in helium that would flood the chamber increasing the pressure and causing a system imaging failure. This issue persisted for around 5 weeks before Dr Langford and I resolved the problem.

A full re-calibration of the motorized helium leak valve finally fixed the regularization of the helium bringing it back to $2.00E-6$ Torr. At this time, I moved over to using the Helios

system and occasionally used the Orion system for Ne-IBID.

5 Results

The results broadly reflect the progression of the experiment and are categorized by key processes. Red annotations on images are from the Orion software whilst green annotations are from the Helios imaging software. Orange annotations have been added to label and clarify scale bars.

5.1 Initial FIB testing

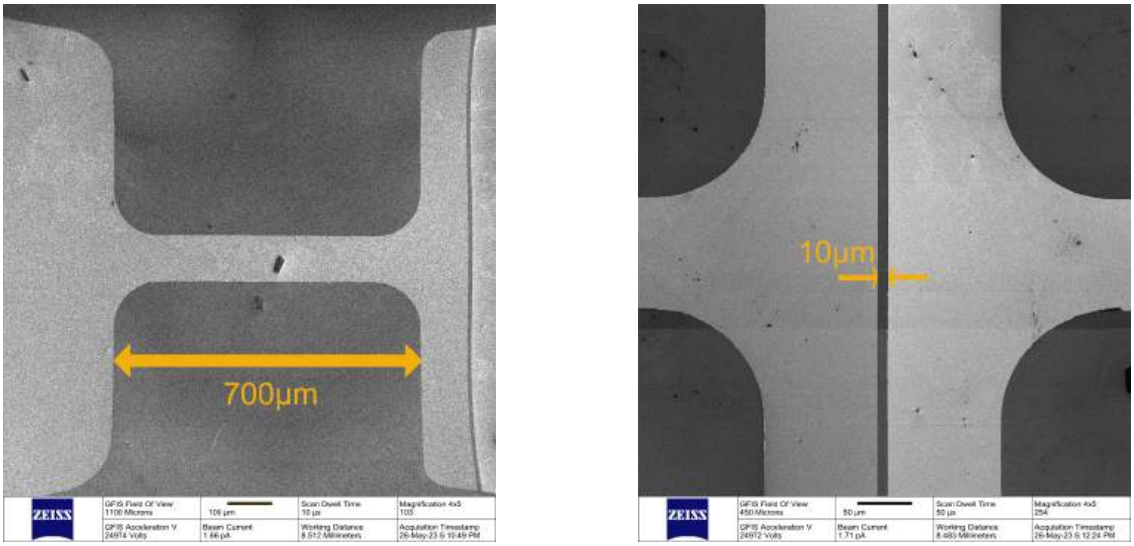

(a) 103x magnification **(b)** 254x magnification

Figure 21: $10\mu m$ gap imaged using big hole aperture, helium ion beam

Initial imaging using the Helium ion beam was largely successful. Figure 21 shows an image of two platinum electrodes on one of the OFET chips. Numbers beside the electrodes dictate the nominal gap between electrodes, in this case $10\mu m$. The accuracy of these values varied between chips, but the gaps were consistently smaller than the proposed size (for instance, the actual size of this gap was $9.15\mu m$). A standard deviation of 10% was observed in gap sizes across chips. The quality of the OFET channel lengths varied due to the lithography process occasionally leaving high boundaries between the substrate and the platinum electrodes. This inhibited the nanowire deposition in multiple ways, discussed later in Section6.

Figure 22 shows an up-close image of this gap. In general, the edges of the electrodes were well defined however a select few had material that crossed the micro-gaps between electrodes. This issue characterised fewer than 10

Imaging with ion beams causes damage to the sample at high magnifications. This enables the

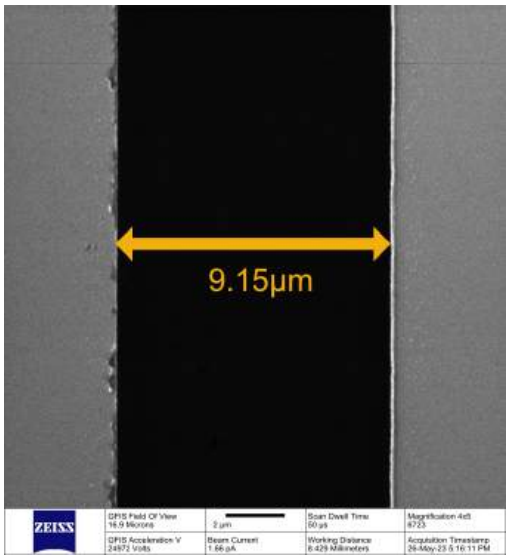

Figure 22: $10\mu m$ gap imaged with big hole aperture, helium ion beam, 6723x magnification

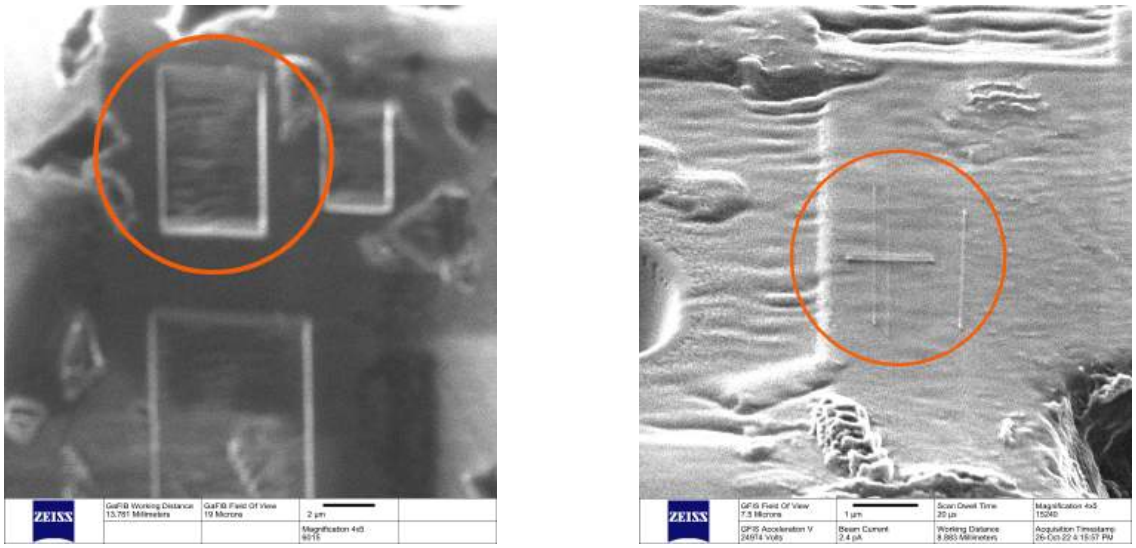

(a) Gallium beam milling

(b) Test of nanowire fabrication with tungsten precursor

Figure 23: Gallium ion beam damage

system to mill away at the surface of specimens, but can also cause unwanted removal of the surface of the electrode. An example of this is shown in Figure 23a where the square patches are indents from the milling process. Figure 23b shows some initial nanowire fabrication tests using the tungsten precursor gas. These are around $2\mu m$ long and $< 50nm$ in width.

For optimal imaging, a landing energy $25kV$ and above was used, with $He20\mu m$ aperture and ideally a beam current of $> 3pA$. For optimal deposition, smaller apertures were utilized such as $He10\mu m$.

5.2 Nanowire Fabrication

Across all samples over 40 sets of electrodes were tested/used for fabrication. Not all potential electrodes were used on each chip for numerous reasons. Typically, one chip was used for deposition whilst voltage testing was done on another. This was to improve workflow and reduce the number of times each chip was transferred from each system (a relatively time-consuming process). Furthermore, the specimen was not always laid perfectly horizontal – by working in columns or rows this became less of an issue. Of these sets, over 30 were successfully tested to show the presence of nanowires.

5.2.1 Platinum wire fabrication using helium and neon ion beams

The nanowires were not typically imaged after fabrication. This was to prevent any further deposition of the adhered platinum gas that may reside on the surface of the specimen as well as any unwanted damage to the wire. Test wires were fabricated during every session before fabrication on a set of electrodes. These were imaged to determine the success of the FIB, with examples shown in Figure 24. Here, different dosages were tested for nanowire fabrication.

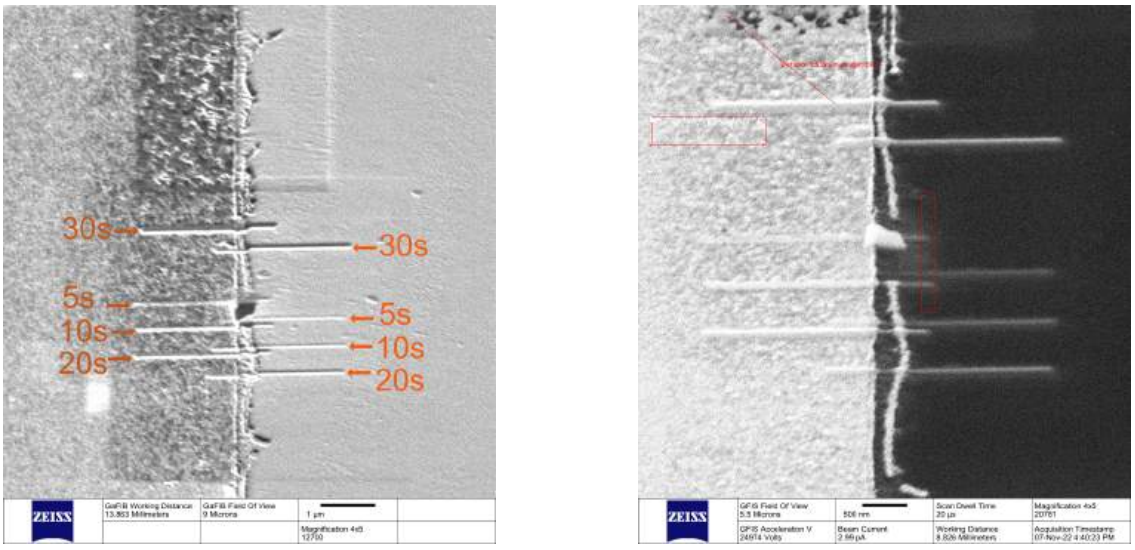

(a) Gallium FIB imaging **(b)** Helium FIB imaging

Figure 24: Dosage testing for nanowire fabrication

The orange annotations detail the total dosage time to form the observed nanowires. Four different dosages were tried twice each, giving the eight lines seen in Figure 24. Each line was $2.5\mu m$ long. Both images in the figure are of the same lines but at different angles. Figure 24a was imaged using the gallium FIB from the Orion system with the sample at 45° towards FIB. Figure 24b is at 45° away from the helium column. The nanowires are all similar widths of 65nm however vary in depth. It was apparent in this test the 20-second dwell time wires had the desired thickness of 50nm. Since this dosage time is only applicable

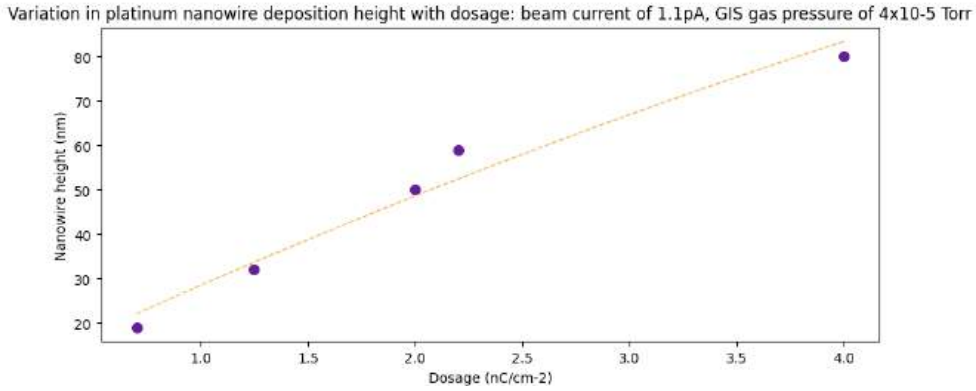

Figure 25: Plot of nanowire thickness according to dose for nanowires

to wires $2.5\mu m$ long, a more usable measurement is the corresponding dosage of $2.5nC/cm^2$. It became evident this dosage is influenced by the focus and alignment of the FIB meaning in practice a dosage of $2 - 4nC/cm^2$ was used depending on the degradation of the trimer and beam shift/tilt that provided the optimal focus for that specific session.

Figure 25 shows how nanowire thickness corresponds to ion-beam dosage. This process is further dependant on the ion-beam current and the precursor gas pressure, thus requiring fine-tuning for each session.

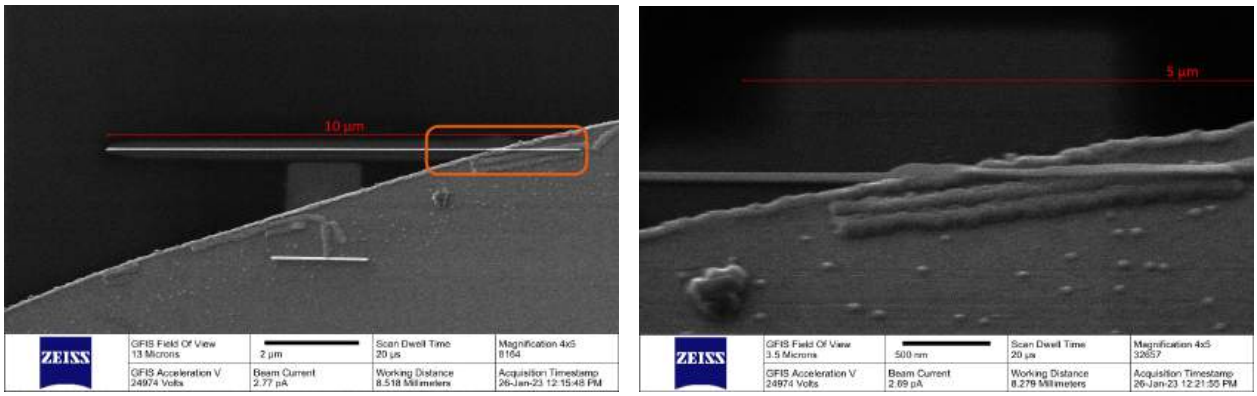

(a) 0° tilt **(b)** 45° tilt

Figure 26: Test wire, helium ion beam, $10\mu m$

Figure 26 shows a high-resolution, long dwell time scan of some test wires; these being the thin white lines on the image. A longer dwell time provides a better image as the ETD values are averaged over an increased period. Figure 26b shows the section of the wire highlighted in orange at a 45° tilt. Here you can see the ridge of the wire as it passes over the edge of the electrode. This suggests that the wires are laid across the substrate rather than being free-standing – a result of the ion-beam scanning process and adsorbed precursor gas molecules. The lighter region lying around the nanowire (often known as a 'halo') is also notable, resulting from interactions between backscattered electrons and the adsorbed precursor molecules [24]. The conductivity of the 'halos' varies depending on the structure formed, however, no significant leakage was observed throughout testing via these regions.

Resistances for thick nanowires (500nm width, 200nm height and greater) have been reported on the scale of $100k\Omega$ [25]. The nanowires in this image are approximately 50nm wide, and <50nm thick (measurements made from viewing at multiple angles).

Figure 27 shows an example of a nanowire crossing the electrodes. Here you can see the capabilities of the Orion system in depositing sufficient wires.

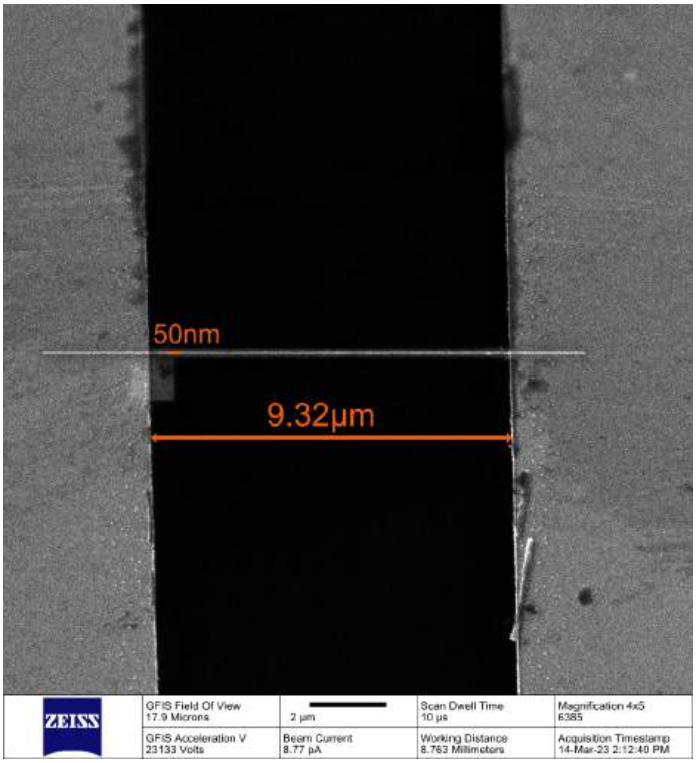

Figure 27: He-FIB platinum nanowire across "$10\mu m$" gap

5.2.2 Platinum wire fabrication using gallium ion beam

Nanowires were fabricated at a greatly increased rate with the Helios system. This was a result of the more user-friendly software, integrated systems and faster processes.

Figure 28a shows a typical nanowire formed by the Ga-FIB. This image was taken at a 30° angle. Approximated dimensions of the wire are a width of 80nm and a height of 60nm. The larger dimensions from Ga-FIB processes are, broadly speaking, a result of the larger ions. Figure 28b shows a Ga-FIB image of a test wire using the Helios system, demonstrating the limits of the nanowire dimensions at just over 70nm width.

Some alternative designs were tested in the latter parts of the project to ensure proper contact was made with the electrodes, aiming to improve any annealing process of the ends of the platinum wires and the platinum electrodes. One method tried was by laying out two larger rectangles over the electrodes and then a narrow line between these two rectangles.

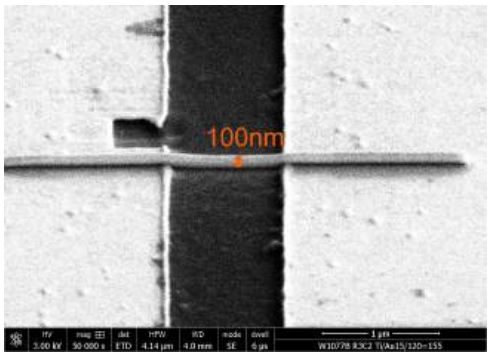

(a) SEM image of nanowire, bridging $2\mu m$ gap, using gallium IBID

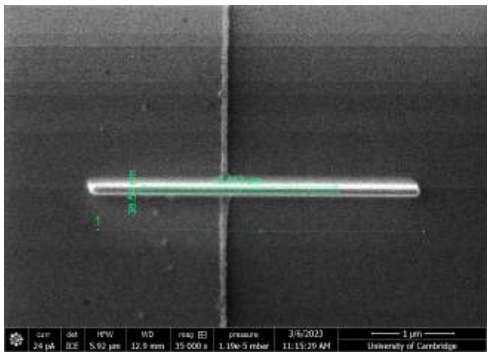

(b) Ga-FIB image of test nanowire, using gallium IBID

Figure 28: Typical nanowire structures using Ga-FIB, Helios system

This pattern had to be done in parallel, a single ion beam pass covers the whole pattern, to prevent any stacking of structures and ensure the deposition was fully connected. An example of this is shown in Figure 29.

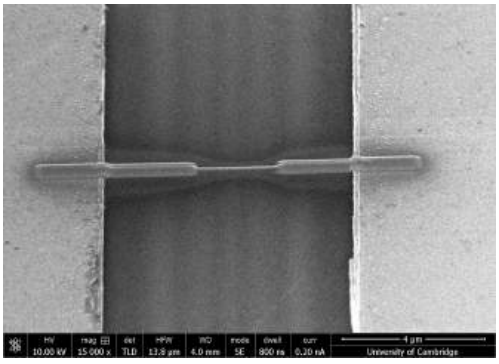

(a) 30° angle

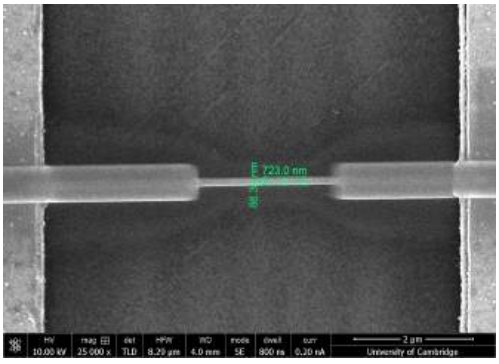

(b) vertical

Figure 29: Ga-FIB nanowire, alternate design, $6\mu m$ gap

5.2.3 Nanowire characteristics

The resistances, deposition methods and dimensions of the most notable nanowires are shown in Table 1.

This indicates that there is a linear relationship between nanowire lengths and observed resistance, as expected. Ga-FIBID wires were often thicker than He-FIBID wires but had similar resistances for equal lengths. This suggests Ga-FIBID wires have a high resistivity than He-FIBID wires.

Rough estimates of resistivity can be calculated using equation 2 which takes the area as the form of a 'thickened' Gaussian [20], σ is set as 1/4 the observed nanowire width, R is the measured resistance, L is the measured nanowire length. The shapes used in these calculations were informed by Figure 30, with the calculated areas shown in Figure 31. Since

FIB method	width(nm)	height(nm)	length(μm)	Resistance
Gallium	80	50	1500	$2k\Omega$
Helium	50	40	2000	$5k\Omega$
Helium	50	45	2000	$400k\Omega$ no annealing
Neon	95	40	2000	$140k\Omega$
Gallium	125	40	2000	$1.8k\Omega$
Gallium	280	40	4000	$3k\Omega$
Gallium	180	40	4000	$4k\Omega$
Neon	90	40	4000	$64k\Omega$
Helium	50	50	6000	$600k\Omega$ no annealing
Gallium	200	40	6000	$4k\Omega$
Gallium	200	40	6000	$5k\Omega$
Gallium	170	45	8000	$7k\Omega$
Gallium	200	50	8000	$7k\Omega$
Gallium	200	40	10000	$8k\Omega$
Gallium	300	50	10000	$10k\Omega$

Table 1: Nanowire characteristics

we are using a two probe setup we also inherently measure the resistance of the electrode plates. These are, however, much smaller than the resistance of the wire.

$$\rho = R/L \int_{-2\sigma}^{2\sigma} \exp -x^2/2\sigma^2 \, dx \tag{2}$$

Estimates from this form give resistivity measurements of around $100\mu\Omega cm$ for He-FIBID and $200 - 350\mu\Omega cm$ for Ga-FIBID. Observations made by Hoffman measure the resistivity wires made using the same precursor and EBID to be around $30\mu\Omega cm$ and when using Ga-FIBID to be around $70 - 140\mu\Omega cm$. [20]

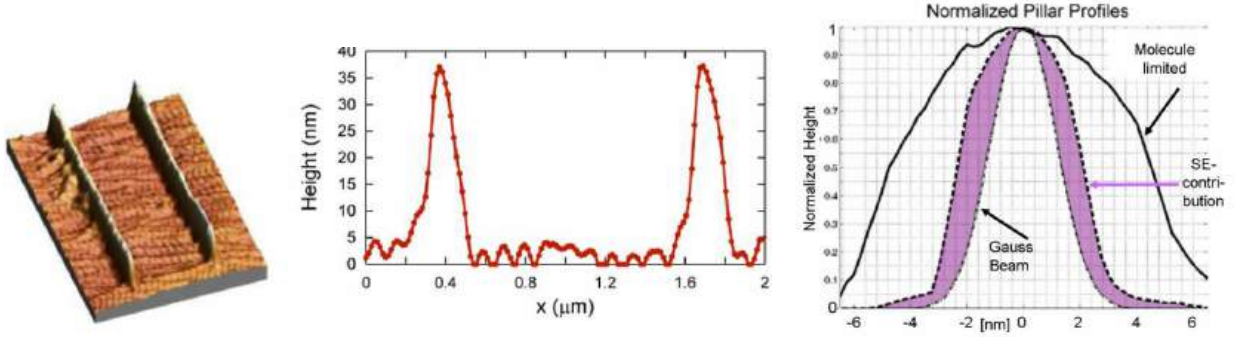

(a) platinum nanowire cross-sections observed using AFM [26]

(b) Hypothesised cross-section using Monte Carlo simulation [20]

Figure 30: Reported nanowire cross-sections

It was observed that for some nanowires issues regarding resistance and failure came from a

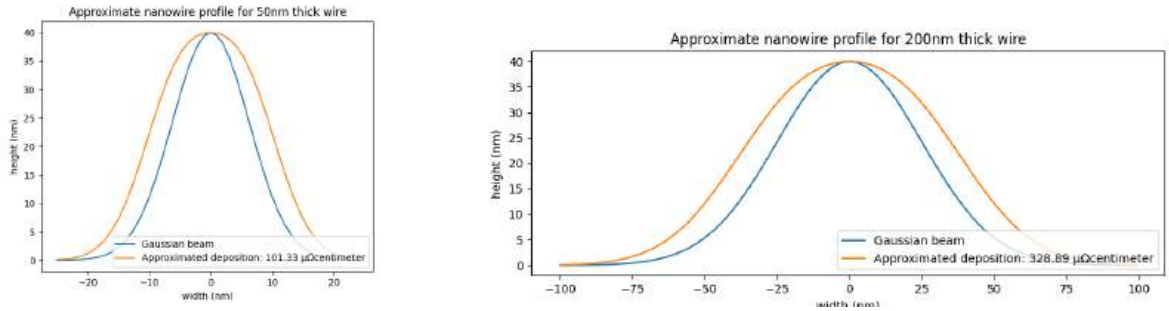

(a) 50nm platinum wire formed via He-FIBID

(b) 200nm platinum wire formed via Ga-FIBID

Figure 31: Approximate nanowire cross-sections based on observations and current literature

combination of the OFET chips topology and OmniGIS probe angle. Figure 32 shows a series of nanowire formations. Typical successful nanowire fabrication formed a connection over the electrode edge like that seen in 32c. As expected, successful wires gave resistances in the order of $k\Omega s$. Due to manufacturing tolerances with the lithography process in the creation of the OFET chips, the height difference between the platinum electrodes and substrate was variable enough to cause separation when depositing platinum. This formed weak connections seen in Figure 32b and 32d. Even attempts in depositing a wider wire at the edges did not always succeed (see Figure 32a). This issue persisted most heavily with wires formed via He-FIBID where thinner wires were deposited. Connections were evidently still made as linear characteristics were often observed, however thinning around these connections meant much larger resistances were observed, in turn affecting nanogap formation as it formed a weak point. It suffers further as a result of the angle of the GIS probe: material which lies in front of the probe received an increased flux of precursor gas, while some sections lie shielded from the gas molecules. This can worsen the effect.

There are multiple solutions to these connectivity issues, including:

- Using an alternative set of electrode chips with thinner platinum electrodes
- Partially eroding the electrode contacts before the deposition to improve the connection
- Utilizing the GIS at various rotations to build up sections where there may be poor connections

5.3 Formation of Nanogaps

Nanogap formation was done via voltage ramps as suggested by Durkan and Hadeed [16]. The rate of change of voltage was nominally set to $4mV/s$, although this varied by step changes on the source measurement unit. This was to try and achieve sufficiently small nanogaps. Nanowires formed via Ga-FIBID generally performed more consistently than those created via He-FIBID. This observation is further discussed in Section 6.

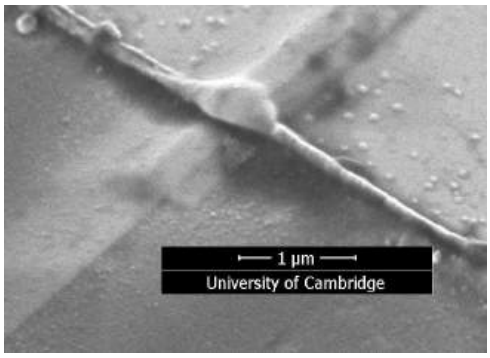

(a) Wide overhang, Ne-FIBID

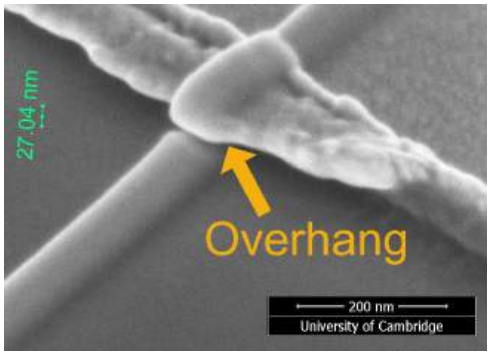

(b) He-FIBID, overhang

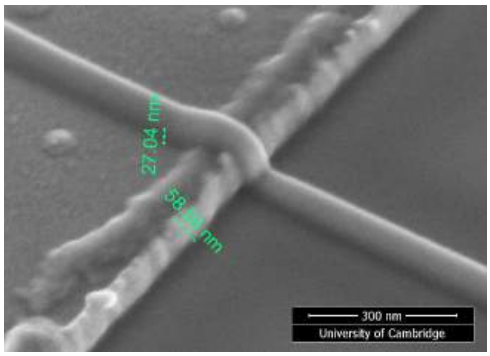

(c) He-FIBID, typical connection

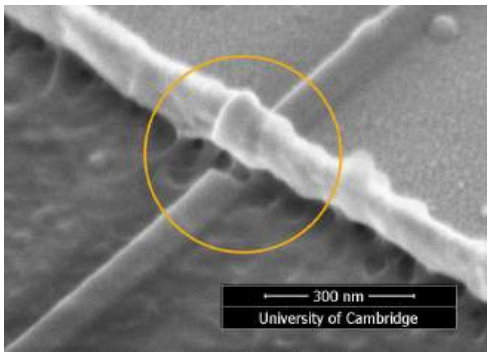

(d) He-FIBID, overhang

Figure 32: Series of test wires imaged using SEM

Although there was no consistent regime before breaking across the samples tested, the data can be categorized into a few different principle plots determined by positive, negative or constant differential conductance. Non-linear characteristics were observed in most but not all cases, likely resulting multiple factors. Appreciable heating is determined by the current and resistances of the wires. Without in situ temperature measurements explanations for I(V) characteristics through the structure's temperature coefficients cannot be determined. The large majority of lines were monotonic before failure. Some showed noisy characteristics at higher voltages suggesting changes to the microstructure.

Focusing on the initial portions of each plot, Figure 33a shows a decreasing resistance, Figure 33b shows an increasing resistance and Figure 33c shows an almost linear resistance. The differential resistances typically drop before failure. This is likely explained by the embedding of the ions from the beam itself. This then creates instabilities for thin wires. For instance, gallium reportedly mixes with gold nanowires giving rise to liquid-like instabilities in sub-30nm wide structures[27].

For wires deposited via He-FIBID the resistance often dropped after applying a slow voltage ramp. This suggests annealing of the contacts to then form a more sufficient connection. It is therefore unclear whether a decreasing resistance with increasing voltage results from electron tunnelling between the platinum electrode and the contact (through the carbon matrix), or comes directly from the wire. This is discussed further in Section 6.

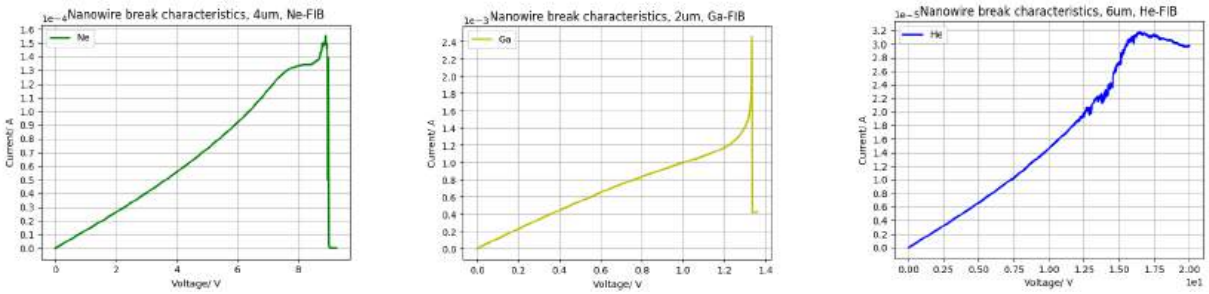

(a) Ne-FIBID **(b)** Ga-FIBID **(c)** He-FIBID

Figure 33: Typical voltage ramps observed

A closer analysis of a plot is shown in Figure 34a, specifically for a platinum wire formed via Ga-FIBID, with a patterned width of 30nm and height of 40nm. In practice, these were observed to be 70nm wide and 40nm tall. Before this, a series of voltage ramps were performed slowly increasing in magnitude until inflexion was observed. A final voltage ramp was then set, stopping shortly after the wire had broken. Observations are as follows: (1) a linear region of the wire with a resistance of $2.4k\Omega$; (2) non-linear characteristics suggesting a positive temperature (provided wire temperature increases with voltage); (3) inflexion representing the drop in resistance just before the wire breaks; and (4) a sharp decrease as the wire breaks to form a nanogap.

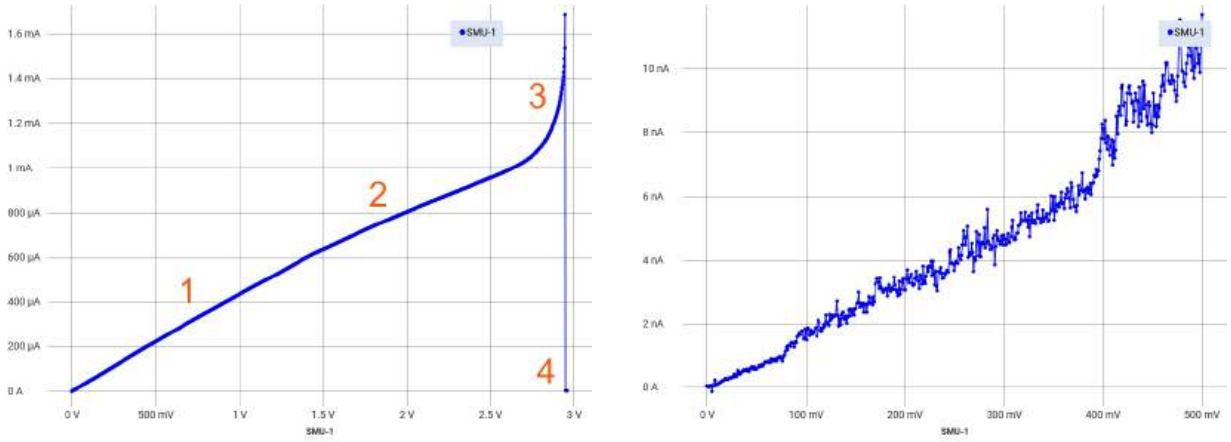

(a) Voltage ramp and nanogap formation, of $2.4k\Omega$ wire **(b)** Characteristics of nanogap

Figure 34: Breaking and characterisation of $4\mu m$ platinum wire formed from Ga-FIBID

Figure 34b shows the expected non-linear characteristics of a nanogap junction. Typical of electron tunnelling there is a linear regime at low voltages (where the nanogap follows Ohm's law) followed by a transition to exponential behaviour. This was consistent between wires, producing good characteristic non-linear electron tunnelling behaviour with varying resistances over 14 sets.

Another regular break is shown in Figure 35. This more closely matches the breakages observed by Hadeed and Durkan [16], suggesting smaller nanogap formation. The principles

of this are further discussed in Section 6.

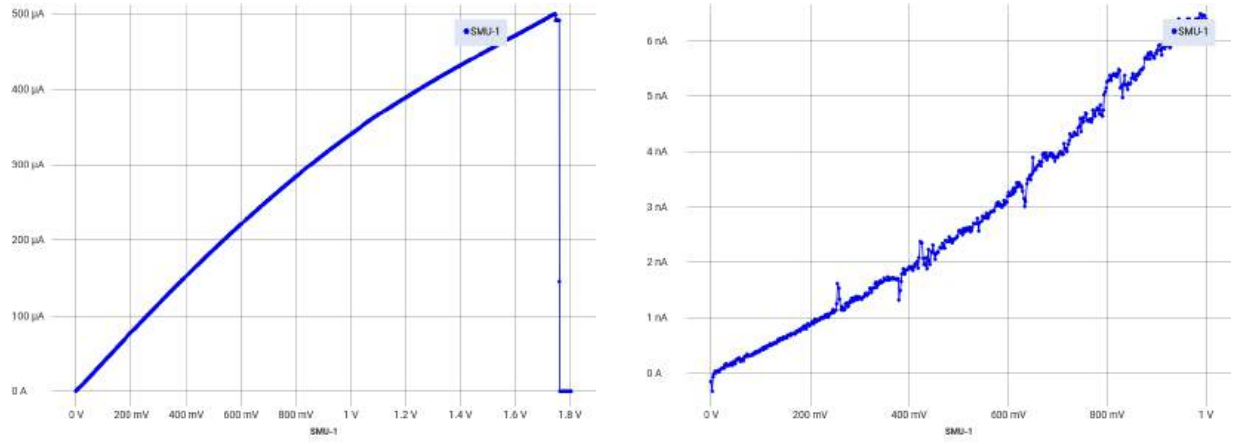

(a) Voltage ramp and nanogap formation, of $2.9k\Omega$ wire

(b) Characteristics of nanogap

Figure 35: Breaking and characterisation of $2\mu m$ platinum wire formed from Ga-FIBID

Once again Figure 35b shows the expected characteristics of electron tunnelling in a nanogap. The resistance observed here is very high, on the order of $100 - 200M\Omega$. This was expected to decrease significantly upon the addition of organic molecules.

Typical nanowire characteristics varied between $2k\Omega$ and $1M\Omega$ before nanogap formation. After formation, resistances varied non-linearly in the order of $M\Omega$ to $G\Omega$. This came from the different parameters used between depositions. He-FIB wires typically had large resistances which dropped after annealing. The GIS was not always uniform, with nanowire height varying between $20nm - 100nm$. Upon mastering the use of the system, these values settles more consistently to 50nm.

5.4 Organic Molecule Insertion

After nanogap formation, multiple sets of electrodes were tested with organic molecule deposition. Figure 36 details the first electrode tested, showing comparisons of the device characteristics before and after adding 1,5 diamino-2-methyl pentane. The hysteresis observed after adding organic molecules produces an increase in differential resistance, indicated by the shallower gradients. This is demonstrated in the two distinct blue lines in Figure 37 for up-sweeps (bottom blue line) and down-sweeps (top blue line). The scales were limited to emphasise this distinction.

The differential conductance of the organic substance curves was also plotted, as shown in Figure 38. These were obtained by separating the upsweep and down-sweep portions of the curve and taking the average plots over 10 runs. The orange lines were fitted after testing. The two curves in this figure are largely symmetric, although there is a slight offset between the minimum points. The notable asymmetry within each plot emphasises the effect of charging behaviours, yet there is no indicator of the desired diode like-characteristics.

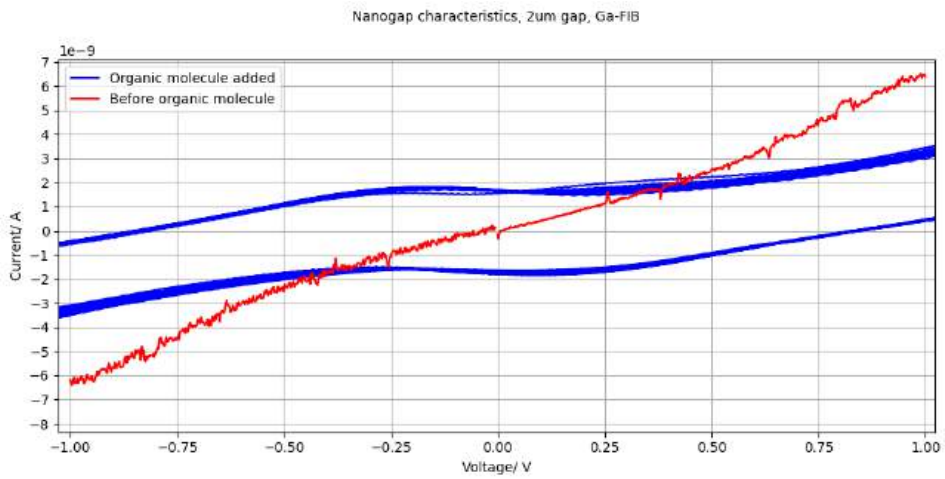

Figure 36: Full sweep after organic molecule addition to $2\mu m$ gap nanowire

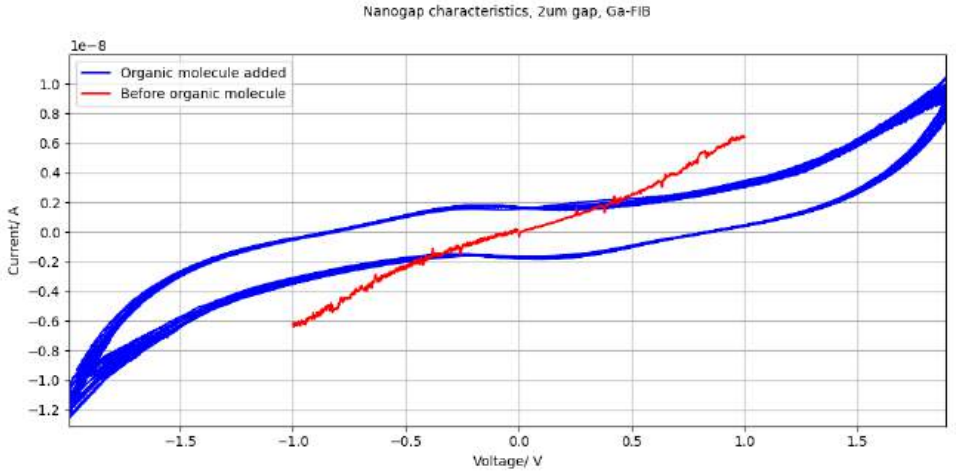

Figure 37: Full sweep after organic molecule addition to $2\mu m$ gap nanowire

The presence of hysteresis is indicative of charge trapping and de-trapping. Whilst the organic molecule used does not possess any obvious charge-trapping sites, the plots indicate that charge-trapping increases the resistance of the structure. This became more evident when a voltage step was applied: the current would peak at the initial step change on each run, peaking at lower currents on each subsequent run. This is further explored in Section 6.

Overall the addition of organic molecules reduced the resistance of the sample, altered the I(V) characteristics, and introduced charging. A large drop in resistance (up to two orders of magnitude) upon the addition of organic substance was expected based on current research [28].

Subsequent tests found similar results with few effects from the addition of molecules into the system. Figure 39 shows that the resistance of the nanogaps increased after the addition of the conductive molecules, suggesting poor that contact was made between the organic molecules and the nanogaps in the wires.

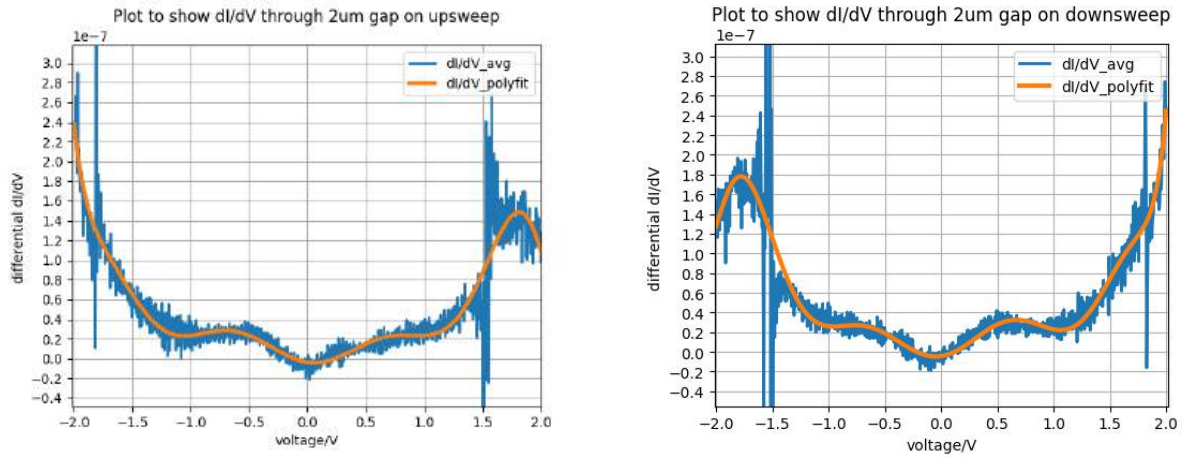

(a) Upsweep characteristics **(b)** Downsweep characteristics

Figure 38: Differential conductance plots of nanogap after organic molecule addition

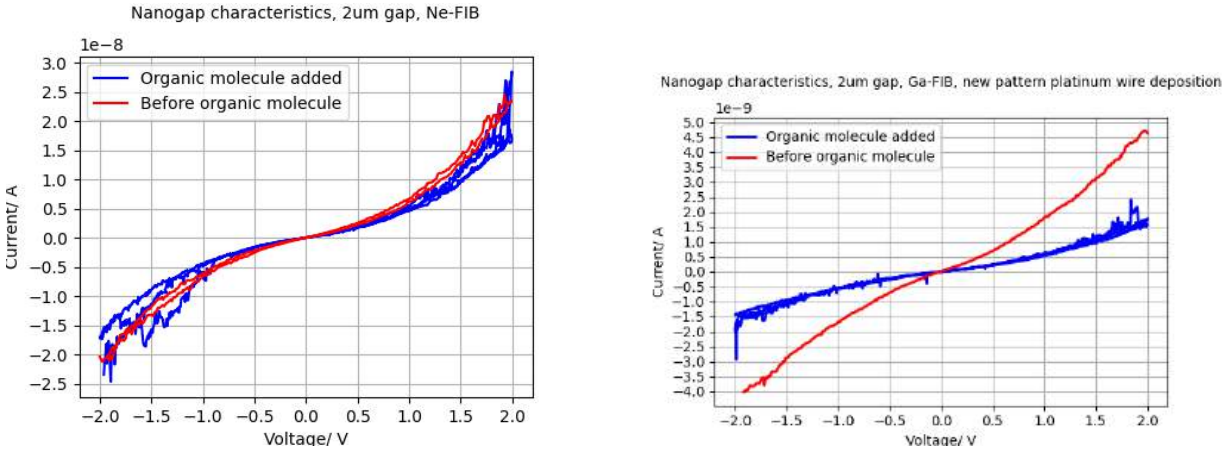

(a) Ne-FIB, 2um platinum wire **(b)** Ga-FIB, 2um platinum wire

Figure 39: I(V) characteristics of nanogaps before and after adding 1,5 diamino-2-methylpentane

5.5 Nanogap imaging

Based on the minor effects organic molecule addition had on the characteristics of the nanogaps, sets of nanogaps were imaged using the SEM to help explain the observations.

Figure 40 shows a series of microstructure formations. It is apparent that structures $> 10nm$ were formed with some catastrophic failure of $200nm$ gaps. Failing of this kind has been observed by Hadeed and Durkan [16] and is likely a result of the melting of the nanowire. Failure was generally observed towards the ends of the wire, although no obvious preference was observed between the cathode and anode side. It is also possible to identify holes forming throughout the body of the wire, indicating melting during the voltage ramp. All images in Figure 40 are of wires formed using Ga-FIBID.

The most promising sample is illustrated in Figure 41, the same wire that produced Figures 35

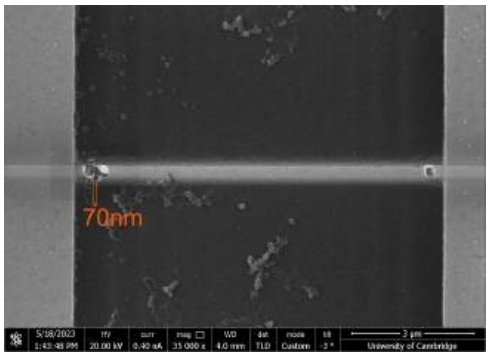

(a) $10\mu m$ wire, failure at 10V

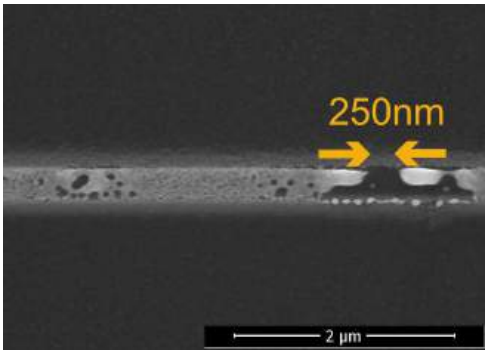

(b) $8\mu m$ wire, failure at 7.7V

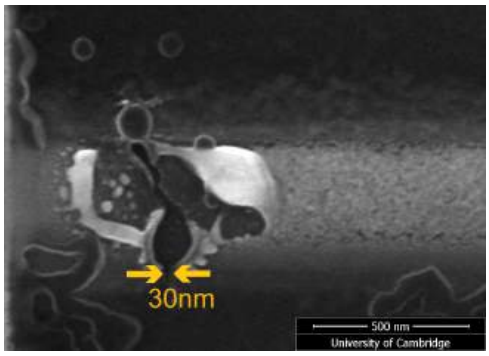

(c) $6\mu m$ wire, failure at 5.4V

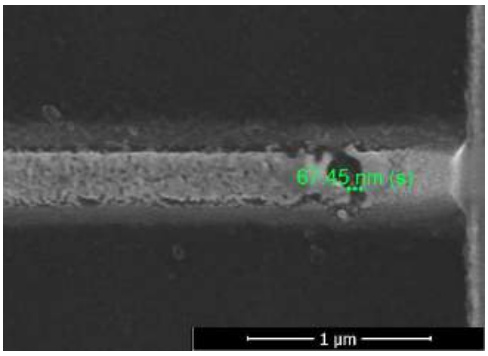

(d) $4\mu m$ wire, failure at 3.4V

Figure 40: Series of wires formed from Ga-FIBID, failed via voltage ramps

and 36. This wire originally had a resistance of $1.8K\Omega$, increasing to an order of $150M\Omega$ once broken. The sample resistance appeared to increase upon the addition of organic molecules. It is possible to observe the uneven halo around the wire, a combination of residual platinum deposition and 1,5 diamino-2-methylpentane. The nanogap in this sample can be observed to be sub-20nm, although the breakpoint is uneven. This may be due to the wire's width, where instabilities in structure lead to failure at various points. The wire broke at what could be a mechanical weak point around the transition between electrode and substrate (seen more clearly in Figure 41b).

6 Discussion and Further Work

6.1 Imaging and nanowire fabrication

Despite facing multiple setbacks the imaging capability using HIM proved to be very good and a strong degree of mastery of the system was obtained. It was capable of imaging 10 nm structures and forming sub-50 nm wires, with neon ion microscopy being slightly worse at imagining 20nm structures. The capabilities listed by Zeiss are sub-10nm structures and 0.5nm image resolution [29]: although these were never fully realised in practice, I believe

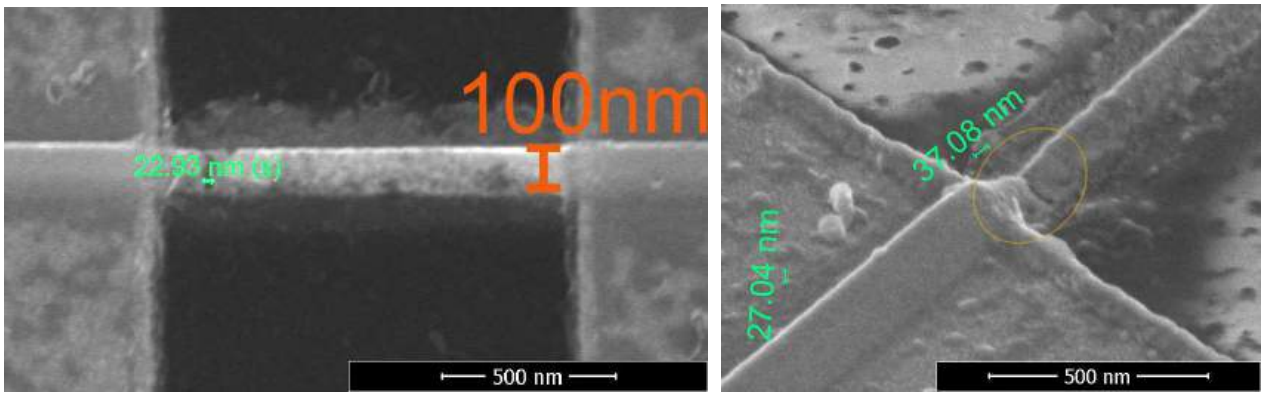

(a) SEM image from above

(b) SEM image at angle

Figure 41: SEM images using Helios system. $2\mu m$ nanowire referenced in Figures 35 and 36,nanowire failure at 1.7V , $500\mu A$

with optimal parameters and an ideal trimer the machine capabilities could come very close to this. This is especially so considering the deposition of platinum was predominantly affected by the OmniGIS system. Hence with optimal parameters and continual servicing, the Orion system would be very sufficient for imaging and forming nanowires and other nanostructures in the future.

The Gallium ion beam, with both the Orion and Helios system, had lower resolution, generally struggling to image sub-30 nm structures. Whilst FEI claim a resolution of 4nm at the coincident point using the Ga-FIB for the Helios nanolab [30], it was observed that wires were consistently above 100nm. This issue was suspected when switching over from the Orion system. The SEM had the most consistent imaging resolution, capable of observing 10nm structures – a similar performance to the HIM at optimal parameters.

Since the Orion system was not under service contract throughout the duration of this year's operation, most issues had to be serviced by Dr Langford and myself. Its operation would therefore benefit from extra details on fixes. I have made some documents regarding the common issues identified throughout this project – paired with Dr Langford's understanding of the machine these should help with any future issues faced by both Master's and PhD students.

Regarding nanowire fabrication, some significant differences were observed with the initial I(V) characteristics between wires formed by Ga-FIBID vs He-FIBID (and Ne-FIBID). It was noted that during the formation of wires via Helium-FIBID, they initially had electron-tunnelling characteristics, while wires formed via Gallium-FIBID showed immediate linear characteristics (at low voltages of 0-200mV). After applying slow voltage ramps to the Helium ion-formed wires they partially annealed and formed better contact with the platinum electrodes. I believe this results from the mechanisms that dominate both forms of FIB. Helium ions

While Helium ions typically penetrate over 100nm into the surface and Galium ions only penetrate 50nm [31], Gallium ions cause more damage to the immediate surface as the platinum film is deposited [32]. This results in an amorphous platinum layer forming beneath the nanowire which also experiences more heating during the deposition process. The combination of these likely explains the better connection between the electrodes and nanowires.

The Orion system is fitted with both a Gas Field Ion Source FIB and Ga-FIB. As such it is possible to lay down the nanowires using the He ion beam and OmniGIS probe, followed by patterning over the ends of the electrodes with the Ga ion beam. I believe this would likely solve the initial annealing with wires formed by He-IBID, which had a partial tendency to fail before forming good contact with the platinum electrodes rendering them unusable.

6.2 Nanogap formation

It became evident towards the end of the project that the nanowire formation in conjunction with single voltage ramps caused various issues for large nanogaps. The difficulties deduced from the results can be split into two main sections: the characteristics of the nanowires (dimensions, composition, microstructure and resistivity) and then the control of voltage ramps.

6.2.1 Wire composition

The experimental composition of the wire from He-IBID is reportedly around 10%-20% [33], giving a resistivity of $25\mu\Omega cm$ [34]. For Ga-IBID composition is heavily dependent on ion current: for instance, one paper observed a resistivity of $70\mu\Omega cm$ under ion beam currents of 220pA [35]. The resistivity is therefore significantly higher with lower beam currents reaching up to $140\mu\Omega cm$. The composition of Ga-FIB wires also varies dependent on ion beam current, which at high levels causes further breakdown of the precursor and removal of carbon to form a purer wire. The resistivity observed in this project's experiments was between $100 - 250\mu\Omega cm$. In contrast, the resistivity of bulk Pt is $10.4\mu\Omega cm$. This observed resistivity may contribute to the failure mode of the nanogaps.

The structure of nanowires formed by FIBID of the platinum precursor consists of an amorphous carbon matrix with intermittent platinum atoms. The classic chemical composition of this is PtC_5, but it has also been hypothesised to be PtC_8. Mass spectra of the product of decomposition revealed the production of CH_3 and H_2 which are pumped out of the system [19]. Ions are also embedded in this wire from the IBID process which varies the resistivity and chemical composition of the wire.

It has been suggested that the platinum wires form a two-phase percolating system[27]. The amorphous carbon can be treated as one phase, as a disordered semiconductor. Platinum is the other, resulting in conductivity at low percentages where there is hopping between defects of metal. When the percentage of platinum increases there is the possibility of conduction

along a continuum moving the I-V characteristics into a metallic regime [36]. This explains the variety of non-linear characteristics observed throughout the project.

Some nanogap breakages were imaged more closely to help deduce the nanowire structure (see Figure 42). It is apparent from Figure 42c that the majority of the melting occurred along the wire bridging the two electrodes. This is reflected in the microstructure studied, over the electrode boundary. The exact transport mechanism that causes melting has not been researched hence information can only be inferred from reports on proposed transport mechanisms during normal operation.

The bulk resistivities of Pt ($10.5\mu\Omega cm$) and Ga ($15\mu\Omega cm$) are far smaller than that of the amorphous carbon ($15,000\mu\Omega cm$). Thus the percolating system is dominated by electron transport between clusters of platinum and gallium atoms [27]. It is reported that the percolating system is influenced by electron tunnelling between metallic nanoparticles. Since electron tunnelling varies exponentially with distance the resistivity of the wire is greatly affected by its composition. Thermal and mechanical stresses caused by differential heating of the substrate (a good insulator) and wire affect the resistivity during the voltage ramp. During the cooling of the wires, it was reported that the interparticle distance increased. This explains the patterns observed in Figure 42 where the platinum (and gallium) clusters appear to merge together to form interstitial droplets.

A proposed formula for resistivity from Naik (2013) is seen in equation 3. Here ρ_0 is the background resistivity of the structure, A is Avogadro's number, v_c is the critical metallic volume concentration (36%) and a relates to the percolation resistivity.

$$\rho = \rho_0 + A|v - v_c|^a \tag{3}$$

This helps us to understand the high dependency of resistivity on the concentration of Pt in the deposited wire. Using the Orion system it was evident nanowires formed from higher beam currents and landing energies generally produced more successful nanowires with lower resistivities. This suggests a higher percentage of Pt which agrees with current literature which proposes an optimal %vol [36].

Figure 42d shows the microstructure around a failure point. It appears that atoms collect in larger regions around the failure point, potentially as a result of the increased heating and hence thermal and mechanical stresses induced in this region. Comparison with images taken using a deposition on a membrane with a Tunnelling Electron Microscope (TEM) (see Figure 43, Platinum ellipsoids are darker in the TEM image), help to illustrate the clusters of platinum atoms within the carbon matrix [37]. It may offer valuable insight to observe the nanogaps formed via electromigration under a TEM to gain a greater understanding of the mechanisms and propose an ideal method of nanogap formation.

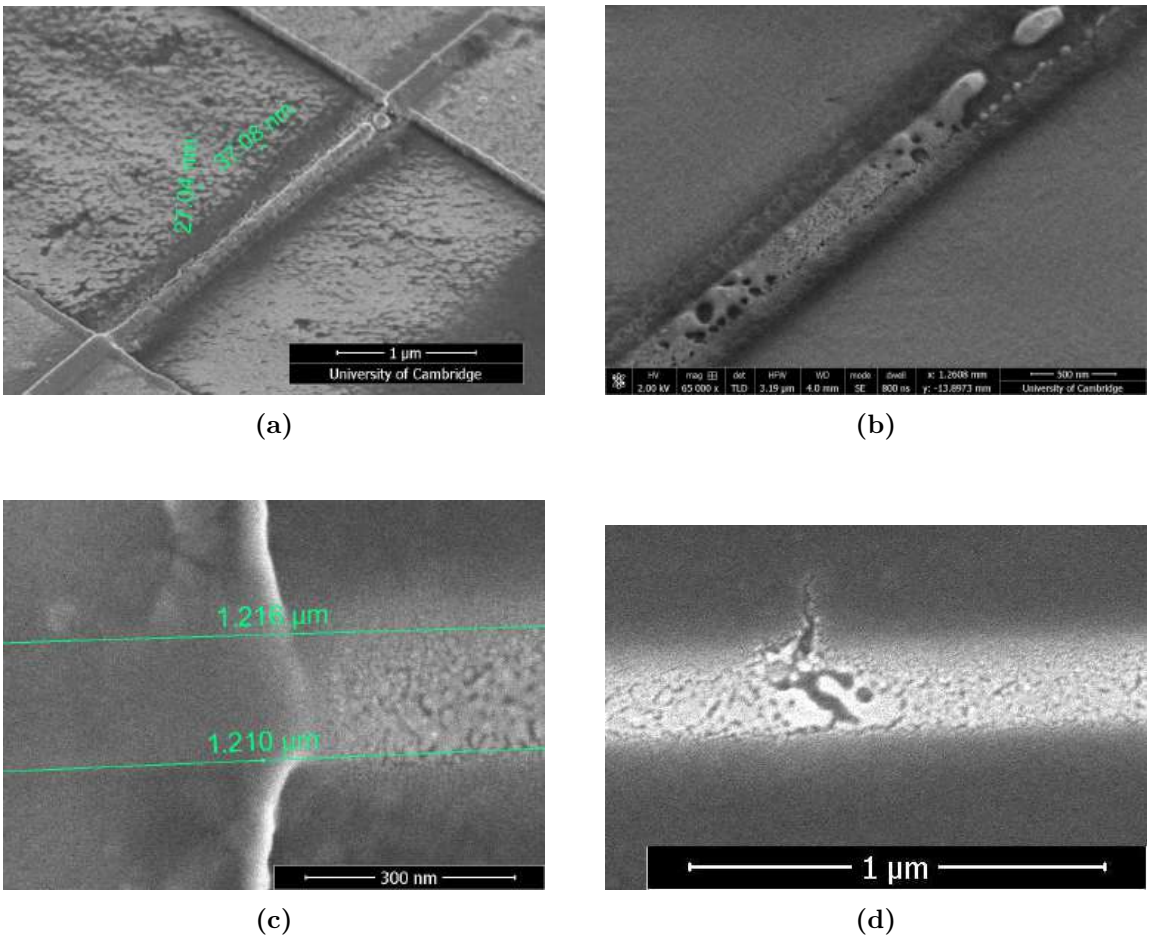

(a) **(b)**

(c) **(d)**

Figure 42: Various nanowire microstructures and Failures, using Ga-FIBID

6.2.2 Voltage ramps

Typical break voltages for the specimens varied between 1.8V-10V. Smaller nanogaps were consistently formed at lower failure voltages, which were also associated with shorter wires. Thus $2\mu m$ nanowires consistently performed better than longer wires.

Figure 34a demonstrates that wires often had an inflexion point before failing. The exact mechanisms determining this are difficult to deduce, however some ideas can be hypothesized. The surrounding literature indicates that deposited platinum wires show non-metallic transport behaviour. This is common in many disordered materials. Reguer and others found that droplets formed during voltage ramp across deposited platinum wires, that remain where they nucleate.[38] Their observation of a negative temperature coefficient (between 0-2V), however, has not been observed in this project. It seems more likely that the linear region 1 is a direct result of typical metal behaviour at room temperature. Then as the wire heats up the resistance increases (2). Based on the images of the nanogaps after the break, there are characteristic signs of melting with droplet formation. These suggest some form of thermal runaway during (3), although this needs further testing.

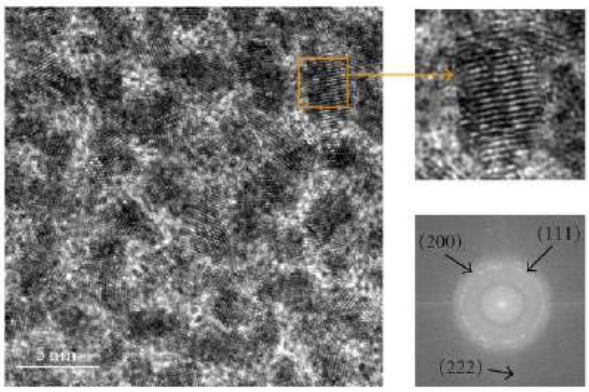

Figure 43: HRTEM images of a Pt nanodeposit by FIBID, 30kV beam energy, on a TEM Cu grid covered with a thin supporting holey carbon membrane [37]

As mentioned earlier, the resistance of nanowires formed via IBID heavily depends on the wire composition since different mechanisms can dominate. For instance, Li, Jin and Tang observed a negative temperature coefficient for Pt/Ga/C nanowires (deposited wires with high content of embedded Ga^+ ions), yet a positive temperature coefficient for Pt/C nanowires. (See Figure 44). While this report covers low-temperature measurements the dependence of composition on resistivity is clear.

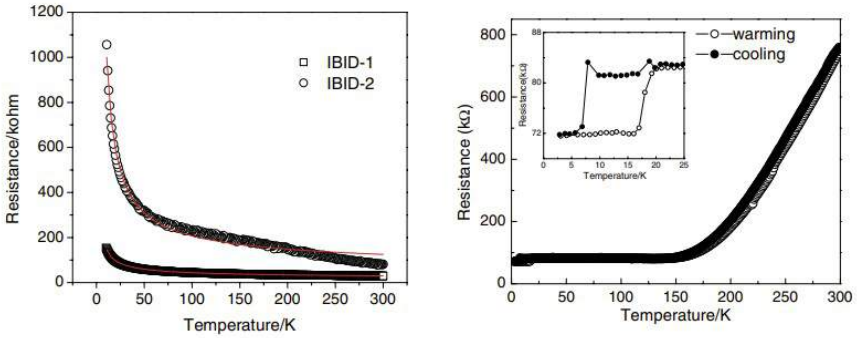

Figure 44: Plots of temperature against resistance for Pt/Ga/C nanowires (left) and Pt/C nanowires (right) [39]

For electromigration to occur large current densities must be induced in the nanowires. The momentum transfer between conducting atoms from large current densities then leads to the drift of atoms causing voids. This mechanism found in pure wires is not the same in the amorphous structure present in nanowires formed via IBID. In gold wires, once the breaking process has begun the current density and heating of the local region increases [40]. An effect akin to this may occur in the platinum nanowires, causing the reduction in resistance before failure. Typically on the I-V plots a constant current at increasing voltage indicates electromigration [41]. Figure 45 shows an example of this. The plot also has non-linear characteristics between 0-7V: it is difficult to determine if this resulted from electron tunnelling between the nanowires and platinum electrodes or the characteristics of the wire itself. Shortly after the suspected onset of electromigration the resistance dropped and the

wire failed via melting.

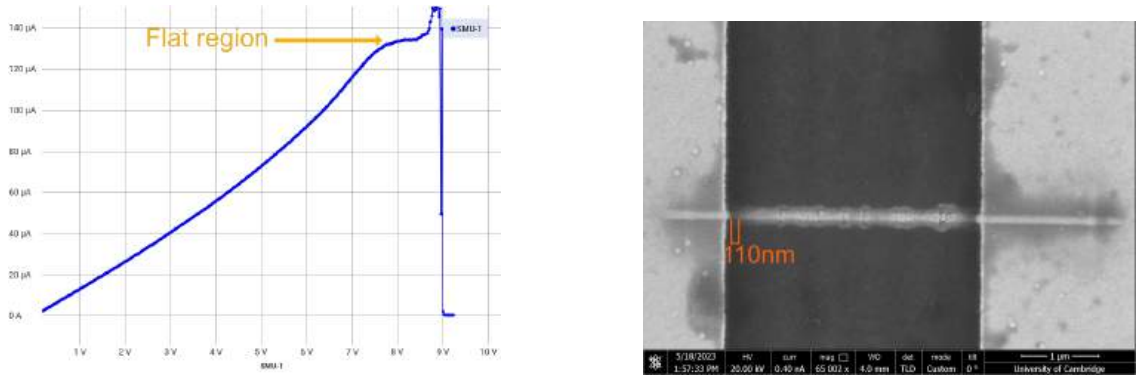

(a) I-V plot of voltage ramp **(b)** SEM image of nanogap

Figure 45: $4\mu m$ nanowire formed via Ne-IBID

These results thus point towards Joule heating failure instead of electromigration. To get 2-3nm gaps lower voltage ramp rates should be tested. The Keithley 2450 source measurement unit was tested with sub 4mV/s rates for a few samples however the failure still provided nanogaps above the desired size. Rates as low as 0.1mV/s may be desirable to reach optimal nanogap size and compensate for the increased resistivity of the wires [42]. There is also potential for feedback-controlled voltage ramps to be used to help determine the feasibility of electromigration in these devices [43]. While this method is not strictly necessary (the combined effect of Joule heating and electromigration observed in gold nanowires successfully forms 2-3nm gaps) it would be good to demonstrate the consistent success of electromigration to form thin nanogaps in platinum wires formed via FIBID. An example of feedback-controlled voltage ramps that could be used are detailed in Figure 46.

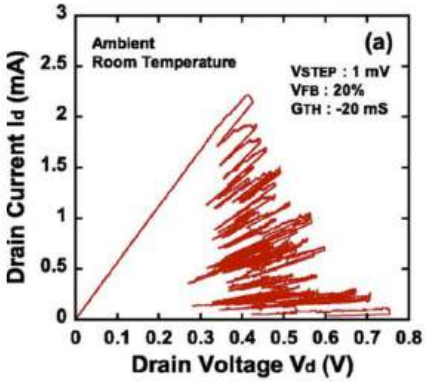

Figure 46: Feedback controlled single ramp [43]

In the experiment that produced Figure 46 rapid response feedback was used, conditioned on a threshold differential conductance. This continual ramping up and down promoted fast electromigration without complete failure.

Beyond altercations to the current method of nanogap formation, there is potential to use the Helium-FIB for the whole process, not just the deposition. Previously this was not

possible due to limitations in the resolution of electron beam lithography, which lies around 5nm[44]. However with HIM the limit is pushed below the 5nm scale. Gaps made via He^+ ion beam milling of electron beam lithography structures have produced nanogaps of 4-5nm size [45]. Furthermore using a 'sketch-and-peel' technique [46], nanogaps below 5nm can be consistently created (see Figure 47).

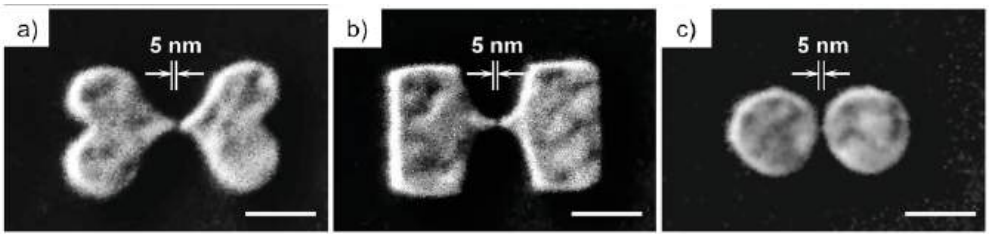

Figure 47: Nanogaps formed via 'sketch and peel' [47]

It has even been possible to form 2-3nm gaps in carbon nanotubes via helium ion sputtering [48]. The average gap sizes observed in this experiment were 2.8 ± 0.6 nm, an order of magnitude more precise than electron beam etching.

Thus the use of solely Helium ion beams for this project could help remove complexities from the electromigration process in a two-phase percolating system – a process which is not yet substantially documented [49]. This does, however, rely on perfect parameters when using the system, determining the exact dwell time, beam current and beam settings to provide the thinnest ion beam. In practice these settings were only achieved a few times throughout the project, such that far more time would need to be spent optimising the use of the Orion system to obtain up to sub 20nm wire thicknesses and 2-3nm gaps.

6.3 Organic molecule deposition

The application used for organic molecule addition was fairly straightforward. There were minor difficulties with localizing the organic molecules to the desired electrodes, often spanning multiple in the process. It was not possible to submerge the electrodes in the organic liquid as in previous experiments. This was because a voltage was applied to the electrodes while applying the liquid, requiring the chip to be placed in the system in Figure 16.

Since the desired characteristics were not observed it is difficult to evaluate the success of the addition process in isolation. 1,5 diamino-2-methyl pentane has been previously proven to provide non-linear I(V) characteristics, so the main concern was the method of bonding between the organic molecules and the wires. It is difficult to determine the exact nature of bonding between the organic molecules, the platinum ions, and the amorphous carbon matrix without further analysis.

The hysteresis observed during voltage sweeps (see Figure 37) appears to result from charge trapping within the organic molecules. This effect has been observed in organic FET devices

[50], and high-k (dielectric constant) gate substances [51]. The dielectric constant of 1,5 diamino-2-methyl pentane is not recorded however 1-amino pentane is known to have a dielectric constant of 4.5, rendering it a high k material since it is greater than the 3.9 dielectric constant of SiO_2, . This indicates possible charge trapping within organic deposits in the structure of the wires. The shape of the hysteresis is time-dependent. Since the voltage sweep had automatically adjusted step times it means the charging was not applied in a linear fashion. This would affect the final shape of the plot.

When initializing the voltage sweep the voltage does a step change to 2V. This fast pulse eliminates the effects of charge trapping as there is insufficient response time. This was observed in multiple runs, and has been observed in literature characterizing gate dielectrics [51]. The observation suggests that the apparent increase in resistance is from charging effects opposing electron flow within the wire rather than a complete re-arrangement to the microstructure. Molecular deposits were seen along the wire and around the 'halo' in the SEM images. There is a possibility that organic molecules have bonded to the uneven nanowire structure after melting, filling voids and bridging gaps. This has the effect of introducing defects that trap charge. Further analysis is required to provide sufficient evidence of this.

7 Conclusions

In conclusion, this project aimed to form molecular devices by investigating the capabilities of FIB technology and evaluating its effectiveness in nanowire deposition and nanogap formation. My results demonstrate successful imaging of various samples using the FIB system, providing high-resolution visualizations of the observed structures.

The nanowire fabrication process using FIB deposition proved successful, yielding well-defined nanowires of the desired dimensions. These fabricated nanowires exhibited promising electrical properties, as indicated by the voltage plots obtained through testing. The successful deposition of nanowires opens up avenues for further exploration and utilisation in various nanoscale applications. Variability in the topology and deposition characteristics would have to be reduced for sufficient yield on a large scale, and could potentially be achieved by parallel patterning of nanowires. The test chips provided some difficulties with uneven overhangs on the electrodes.

Despite success with nanowire fabrication, the formation of nanogaps using voltage ramps proved to be challenging. Even with repeated attempts under different voltage ramp rates and parameters the desired nanogap dimensions were not satisfactorily obtained. The difficulties encountered in nanogap formation highlight the intricacies and technical challenges associated with this process, which necessitate further investigation and optimization.

Moreover, the addition of organic molecules onto the fabricated nanowires using the FIB system did not yield the desired outcomes. The intended functionalization of nanowires with organic materials, aimed at exploring their potential applications in electronic devices, was unsuccessful. This result highlights the need for alternative techniques or approaches to

effectively incorporate organic molecules.

Despite these limitations, the FIB system's successful imaging capabilities and the fabrication of high-quality FIB-deposited nanowires offer valuable insights and open up possibilities for future research. These findings lay strong foundations for further studies of the breaking mechanisms underlying nanogap formation and advancing the field of nanoscale device fabrication.

7.1 Future work

The varied success of the FIB system leaves us with multiple options regarding future research. Further studies in this direction would require extended research on the mechanisms of nanowire failure. In-situ observations of microstructure re-arrangement during failure would likely be useful for this. Using TEM imaging to determine the exact microstructures may also provide further insight, with alternate test chips desirable with thinner electrode contacts. Overall the poor molecule-wire contact and variability seen throughout the project render this approach likely unsuitable for long-term research.

Alternate directions for the fabrication of molecular devices may be more viable. Previous papers utilizing electron beam lithography provided more consistent results in forming nanogaps. There is still potential to utilize helium ion microscopy to either mill nanogaps or promote failure of nanowires at a certain point via milling using the ion beam.

8 Appendix

The risk assessment at the beginning of the project shone a light on two main sources of possible risk. Firstly the focused ion beam systems used in this project operate with high voltages. This poses a risk if contact is made however the system is self-contained and only qualified service engineers from the corresponding firm have access to these parts. Second was the use of the probe station in the nanoscience centre. This involves the manipulation of sharp probes with micropositioners. Direct contact was very rarely made with the probes and when done so much care was taken. Voltages were generally limited to 20V, with mA currents, further mitigating any potential risk from the probe station.

Beyond this, general risk came from using extended computer use so good practice with posture and rest breaks was used.

Overall the risk assessment accurately reflected the potential dangers in the project. The project was low risk under normal operation and most of the potential risks had been mitigated by careful system design. Care was still taken when using all equipment and software throughout the project, and as such there were no further complications.

9 References

[1] Fan Wu, He Tian, Yang Shen, et al. "Vertical MoS2 transistors with sub-1-nm gate lengths". In: *Nature* 603 (Mar. 2022), pp. 259–264. DOI: 10.1038/s41586-021-04323-3.

[2] Ruilong Xie, P. Montanini, K. Akarvardar, et al. "A 7nm FinFET technology featuring EUV patterning and dual strained high mobility channels". In: Dec. 2016, pp. 2.7.1–2.7.4. DOI: 10.1109/IEDM.2016.7838334.

[3] Ajuan Cui, Huanli Dong, and Wenping Hu. "Nanogap Electrodes towards Solid State Single-Molecule Transistors". In: *Small* 11.46 (2015), pp. 6115–6141. DOI: https://doi.org/10.1002/smll.201501283.

[4] Colm Durkan and Qian Zhang. "Towards reproducible, scalable lateral molecular electronic devices". In: *Applied Physics Letters* 105.8 (2014), p. 083504.

[5] J. Bardeen and W. H. Brattain. "The Transistor, A Semi-Conductor Triode". In: *Phys. Rev.* 74 (2 July 1948), pp. 230–231. DOI: 10.1103/PhysRev.74.230.

[6] Robert W Keyes. "Physical limits of silicon transistors and circuits". In: *Reports on Progress in Physics* 68.12 (Sept. 2005), p. 2701. DOI: 10.1088/0034-4885/68/12/R01.

[7] Hyungsub Choi and Cyrus C.M. Mody. "The Long History of Molecular Electronics: Microelectronics Origins of Nanotechnology". In: *Social Studies of Science* 39.1 (2009), pp. 11–50. DOI: 10.1177/0306312708097288.

[8] Max Roser, Hannah Ritchie, and Edouard Mathieu. *Computational capacity of the fastest supercomputers*. Mar. 2023. URL: https://ourworldindata.org/grapher/supercomputer-power-flops.

[9] Fabio D'Agostino. *Short-Channel Effects in MOSFETs*. Dec. 2000. URL: http://www0.cs.ucl.ac.uk/staff/ucacdxq/projects/vlsi/report.pdf.

[10] Yi Zhao, Wenqing Liu, Jiaoyang Zhao, et al. "The fabrication, characterization and functionalization in molecular electronics". In: *International Journal of Extreme Manufacturing* 4.2 (June 2022), p. 022003. DOI: 10.1088/2631-7990/ac5f78.

[11] Ryan C. Chiechi, Emily A. Weiss, Michael D. Dickey, et al. "Eutectic Gallium–Indium (EGaIn): A Moldable Liquid Metal for Electrical Characterization of Self-Assembled Monolayers". In: *Angewandte Chemie International Edition* 47.1 (2008), pp. 142–144. DOI: https://doi.org/10.1002/anie.200703642.

[12] Richard L. McCreery. "Carbon-Based Molecular Junctions for Practical Molecular Electronics". In: *Accounts of Chemical Research* 55.19 (2022). PMID: 36137180, pp. 2766–2779. DOI: 10.1021/acs.accounts.2c00401.

[13] Jan Overbeck. *Mechanically controlled break junctions*. URL: https://calame.unibas.ch/research/mcbj/.

[14] J.R. Black. "Electromigration—A brief survey and some recent results". In: *IEEE Transactions on Electron Devices* 16.4 (1969), pp. 338–347. DOI: 10.1109/T-ED.1969.16754.

[15] C Durkan and M.E Welland. "Analysis of failure mechanisms in electrically stressed gold nanowires". In: *Ultramicroscopy* 82.1 (2000), pp. 125–133. ISSN: 0304-3991. DOI: https://doi.org/10.1016/S0304-3991(99)00133-3.

[16] F. O. Hadeed and C. Durkan. "Controlled fabrication of 1–2nm nanogaps by electromigration in gold and gold-palladium nanowires". In: *Applied Physics Letters* 91.12 (Sept. 2007). 123120. ISSN: 0003-6951. DOI: 10.1063/1.2785982.

[17] W. F. van Dorp, J. D. Wnuk, J. M. Gorham, et al. "Electron induced dissociation of trimethyl (methylcyclopentadienyl) platinum (IV): Total cross section as a function of incident electron energy". In: *Journal of Applied Physics* 106.7 (Oct. 2009). ISSN: 0021-8979. DOI: 10.1063/1.3225091.

[18] Sarah Engmann, Michal Stano, Štefan Matejčík, et al. "Gas phase low energy electron induced decomposition of the focused electron beam induced deposition (FEBID) precursor trimethyl (methylcyclopentadienyl) platinum(iv) (MeCpPtMe3)". In: *Phys. Chem. Chem. Phys.* 14 (42 2012), pp. 14611–14618. DOI: 10.1039/C2CP42637D.

[19] Mohammed K. Abdel-Rahman, Patrick M. Eckhert, and D. Howard Fairbrother. "Ion-Induced Surface Reactions and Deposition of Trimethyl(methylcyclopentadienyl)platinum(IV)". In: *The Journal of Physical Chemistry C* 126.37 (2022), pp. 15724–15735. DOI: 10.1021/acs.jpcc.2c05255.

[20] Ivo Utke, Patrik Hoffmann, and John Melngailis. "Gas-assisted focused electron beam and ion beam processing and fabrication". In: *Journal of Vacuum Science and Technology B: Microelectronics and Nanometer Structures Processing, Measurement, and Phenomena* 26.4 (Aug. 2008), pp. 1197–1276. ISSN: 1071-1023. DOI: 10.1116/1.2955728.

[21] URL: https://www.ossila.com/products/prefabricated-platinum-ofet-test-chips?variant=28807381761.

[22] B W Arey, V Shutthanandan, and W Jiang. *Helium Ion Micros copy versus Scanning Electron Microscopy*. 2010. URL: https://www.microscopy.org/MandM/2010/arey.pdf.

[23] Annalena Wolff. *Focused Ion Beams: An overview of the technology and its capabilities*. May 2020. URL: https://analyticalscience.wiley.com/do/10.1002/was.00070009.

[24] Ivo Utke, Patrik Hoffmann, and John Melngailis. "Gas-assisted focused electron beam and ion beam processing and fabrication". In: *Journal of Vacuum Science and Technology B: Microelectronics and Nanometer Structures* 26 (Aug. 2008), pp. 1197–1276. DOI: 10.1116/1.2955728.

[25] D Brunel, D Troadec, D Hourlier, et al. 2011. URL: https://hal.archives-ouvertes.fr/hal-00603003/document.

[26] Patricia Peinado, Soraya Sangiao, and José M. De Teresa. "Focused Electron and Ion Beam Induced Deposition on Flexible and Transparent Polycarbonate Substrates". In: *ACS Nano* 9.6 (2015). PMID: 26035337, pp. 6139–6146. DOI: 10.1021/acsnano.5b01383.

[27] JAY PRAKASH NAIK. *Nanowires fabricated by focused Ion Beam*. Aug. 2013. URL: https://core.ac.uk/reader/18614361.

[28] Subhasis Ghosh, Henny Halimun, Ajit Kumar Mahapatro, et al. "Device structure for electronic transport through individual molecules using nanoelectrodes". In: *Applied Physics Letters* 87.23 (Dec. 2005). 233509. ISSN: 0003-6951. DOI: 10.1063/1.2140470.

[29] Dec. 2013. URL: https://www.london-nano.com/services/equipment/carl-zeiss-orion-nanofab.

[30] Jan. 2012. URL: http://www.labsoft.pl/wordpress/wp-content/uploads/2013/08/Helios-NanoLab-650-ds-web.pdf.

[31] John Notte, Bill Ward, Nick Economou, et al. "An Introduction to the Helium Ion Microscope". In: *AIP Conference Proceedings* 931.1 (Sept. 2007), pp. 489–496. ISSN: 0094-243X. DOI: 10.1063/1.2799423. eprint: https://pubs.aip.org/aip/acp/article-pdf/931/1/489/11625567/489_1_online.pdf. URL: https://doi.org/10.1063/1.2799423.

[32] Adam W. Thompson, Zachary D. Harris, and James T. Burns. "Examination of focused ion beam-induced damage during platinum deposition in the near-surface region of an aerospace aluminum alloy". In: *Micron* 118 (2019), pp. 43–49. ISSN: 0968-4328. DOI: https://doi.org/10.1016/j.micron.2018.12.004.

[33] Colin A. Sanford, Lewis Stern, Louise Barriss, et al. "Beam induced deposition of platinum using a helium ion microscope". In: *Journal of Vacuum Science and Technology B: Microelectronics and Nanometer Structures Processing, Measurement, and Phenomena* 27.6 (Dec. 2009), pp. 2660–2667. ISSN: 1071-1023. DOI: 10.1116/1.3237095.

[34] Po-Shuan Yang, Zheng-da Huang, Kuei-Wen Huang, et al. "Selective growth of platinum nanolines by helium ion beam induced deposition and atomic layer deposition". In: *Ultramicroscopy* 211 (2020), p. 112952. ISSN: 0304-3991. DOI: https://doi.org/10.1016/j.ultramic.2020.112952.

[35] Tao Tao, Jae-Sang Ro, John Melngailis, et al. "Focused ion beam induced deposition of platinum". In: *Journal of Vacuum Science and Technology B: Microelectronics and Nanometer Structures* 8 (Dec. 1990), pp. 1826–1829. DOI: 10.1116/1.585167.

[36] Amalio Fernández-Pacheco, José De Teresa, Rosa Córdoba, et al. "Metal-insulator transition in Pt-C nanowires grown by focused-ion-beam-induced deposition". In: *Physical Review B* 79 (May 2009). DOI: 10.1103/PhysRevB.79.174204.

[37] J. M. De Teresa, R. Córdoba, A. Fernández-Pacheco, et al. "Origin of the Difference in the Resistivity of As-Grown Focused-Ion- and Focused-Electron-Beam-Induced Pt Nanodeposits". In: *Journal of Nanomaterials* 2009 (Apr. 2009), p. 936863. ISSN: 1687-4110. DOI: 10.1155/2009/936863. URL: https://doi.org/10.1155/2009/936863.

[38] A. Reguer, F. Bedu, D. Tonneau, et al. "Structural and electrical studies of conductive nanowires prepared by focused ion beam induced deposition". In: *Journal of Vacuum Science and Technology B: Microelectronics and Nanometer Structures Processing, Measurement, and Phenomena* 26.1 (Jan. 2008), pp. 175–180. ISSN: 1071-1023. DOI: 10.1116/1.2830630.

[39] P. G. Li, A. Z. Jin, and W. H. Tang. "Pt/Ga/C and Pt/C composite nanowires fabricated by focused ion and electron beam induced deposition". In: *physica status solidi (a)* 203.2 (2006), pp. 282–286. DOI: https://doi.org/10.1002/pssa.200521292.

[40] M. Trouwborst, Sense van der Molen, and B.J. Wees. "The role of Joule heating in the formation of nanogaps by electromigration". In: *Journal of Applied Physics* 99 (Nov. 2005). DOI: 10.1063/1.2203410.

[41] Swatilekha Saha, Guoguang Qian, and Kim M. Lewis. "Fabrication of nanogaps by a progressive electromigration technique using wires of various thicknesses". In: *Journal of Vacuum Science and Technology B* 29.6 (Oct. 2011). 061802. ISSN: 2166-2746. DOI: 10.1116/1.3647908.

[42] C. Durkan, M. A. Schneider, and M. E. Welland. "Analysis of failure mechanisms in electrically stressed Au nanowires". In: *Journal of Applied Physics* 86.3 (Aug. 1999), pp. 1280–1286. ISSN: 0021-8979. DOI: 10.1063/1.370882.

[43] Yuma Kanamaru, Masazumi Ando, and Jun-ichi Shirakashi. "Ultrafast feedback-controlled electromigration using a field-programmable gate array". In: *Journal of Vacuum Science and Technology B* 33.2 (Dec. 2014). 02B106. ISSN: 2166-2746. DOI: 10.1116/1.4903929.

[44] A.N. Broers, A.C.F. Hoole, and J.M. Ryan. "Electron beam lithography—Resolution limits". In: *Microelectronic Engineering* 32.1 (1996). Nanotechnology, pp. 131–142. ISSN: 0167-9317. DOI: https://doi.org/10.1016/0167-9317(95)00368-1.

[45] Lisa Seitl, Florian Laible, Simon Dickreuter, et al. "Miniaturized fractal optical nanoantennas defined by focused helium ion beam milling". In: *Nanotechnology* 31.7 (Sept. 2019), p. 075301. DOI: 10.1088/1361-6528/ab5120.

[46] Yiqin Chen, Quan Xiang, Zhiqin Li, et al. ""Sketch and Peel" Lithography for High-Resolution Multiscale Patterning". In: *Nano Letters* 16.5 (2016). PMID: 27074130, pp. 3253–3259. DOI: 10.1021/acs.nanolett.6b00788.

[47] Yiqin Chen, Yueqiang Hu, Jingyi Zhao, et al. "Topology Optimization-Based Inverse Design of Plasmonic Nanodimer with Maximum Near-Field Enhancement". In: *Advanced Functional Materials* 30.23 (2020), p. 2000642. DOI: https://doi.org/10.1002/adfm.202000642.

[48] Cornelius Thiele, Henning Vieker, André Beyer, et al. "Fabrication of carbon nanotube nanogap electrodes by helium ion sputtering for molecular contacts". In: *Applied Physics Letters* 104.10 (Mar. 2014). 103102. ISSN: 0003-6951. DOI: 10.1063/1.4868097.

[49] R. Hoffmann-Vogel. "Electromigration and the structure of metallic nanocontacts". In: *Applied Physics Reviews* 4.3 (Aug. 2017). 031302. ISSN: 1931-9401. DOI: 10.1063/1.4994691.

[50] Somi Kim, Hochen Yoo, and Jaeyoung Choi. "Effects of Charge Traps on Hysteresis in Organic Field-Effect Transistors and Their Charge Trap Cause Analysis through Causal Inference Techniques". In: *Sensors* 23.4 (2023). ISSN: 1424-8220. DOI: 10.3390/s23042265. URL: https://www.mdpi.com/1424-8220/23/4/2265.

[51] Chadwin Young, Dawei Heh, Rino Choi, et al. "The Pulsed Id-Vg methodology and Its Application to the Electron Trapping Characterization of High-? gate Dielectrics". In: *JSTS:Journal of Semiconductor Technology and Science* 10 (June 2010). DOI: 10.5573/JSTS.2010.10.2.079.